



MULTIWAVELENGTH STUDY OF THE STAR FORMATION IN THE S237 H II REGION

L. K. DEWANGAN¹, D. K. OJHA², I. ZINCHENKO³, P. JANARDHAN¹, AND A. LUNA⁴¹Physical Research Laboratory, Navrangpura, Ahmedabad-380 009, India; lokeshd@prl.res.in²Department of Astronomy and Astrophysics, Tata Institute of Fundamental Research, Homi Bhabha Road, Mumbai 400 005, India³Institute of Applied Physics of the Russian Academy of Sciences, 46 Ulyanov st., Nizhny Novgorod 603950, Russia⁴Instituto Nacional de Astrofísica, Óptica y Electrónica, Luis Enrique Erro # 1, Tonantzintla, Puebla, C.P. 72840, México

Received 2016 September 23; revised 2016 October 21; accepted 2016 October 26; published 2016 December 27

ABSTRACT

We present a detailed multiwavelength study of observations from X-ray, near-infrared, and centimeter wavelengths to probe the star formation processes in the S237 region. Multiwavelength images trace an almost sphere-like shell morphology of the region, which is filled with the 0.5–2 keV X-ray emission. The region contains two distinct environments—a bell-shaped cavity-like structure containing the peak of 1.4 GHz emission at center, and elongated filamentary features without any radio detection at edges of the sphere-like shell—where *Herschel* clumps are detected. Using the 1.4 GHz continuum and ¹²CO line data, the S237 region is found to be excited by a radio spectral type of B0.5V star and is associated with an expanding H II region. The photoionized gas appears to be responsible for the origin of the bell-shaped structure. The majority of molecular gas is distributed toward a massive *Herschel* clump ($M_{\text{clump}} \sim 260 M_{\odot}$), which contains the filamentary features and has a noticeable velocity gradient. The photometric analysis traces the clusters of young stellar objects (YSOs) mainly toward the bell-shaped structure and the filamentary features. Considering the lower dynamical age of the H II region (i.e., 0.2–0.8 Myr), these clusters are unlikely to be formed by the expansion of the H II region. Our results also show the existence of a cluster of YSOs and a massive clump at the intersection of filamentary features, indicating that the collisions of these features may have triggered cluster formation, similar to those found in the Serpens South region.

Key words: dust, extinction – H II regions – ISM: clouds – ISM: individual objects (Sh 2–237) – stars: formation – stars: pre-main sequence

1. INTRODUCTION

Massive stars ($\gtrsim 8 M_{\odot}$) produce a flood of ultraviolet (UV) photons, radiation pressure, and drive strong winds, which allow them to interact with the surrounding interstellar medium (ISM). In star-forming regions, the radio and infrared observations have revealed the ring/shell/bubble/filamentary features surrounding the H II regions associated with the OB stars, indirectly tracing the signatures of the energetics of powering sources (e.g., Deharveng et al. 2010; Watson et al. 2010; Dewangan et al. 2016). However, the physical processes of their interaction and feedback in their vicinity are still poorly understood (Zinnecker & Yorke 2007; Tan et al. 2014). In recent years, with the availability of *Herschel* observations, the study of initial conditions of cluster formation toward the filaments, in particular, has received much attention in star formation research. However, the role of filaments in the formation of dense massive star-forming clumps and clusters is still a matter of debate (e.g., Myers 2009; Schneider et al. 2012; Nakamura et al. 2014; Tan et al. 2014).

Located at a distance of 2.3 kpc (Pandey et al. 2013; Lim et al. 2015), the star-forming region Sh 2-237 (hereafter S237; also known as NGC 1931/IRAS 05281+3412/RAFGL 5144/G173.9+0.3; $\alpha_{2000} = 05^{\text{h}} 31^{\text{m}} 22^{\text{s}}.8$, $\delta_{2000} = +34^{\circ} 13' 59''$) has a broken or incomplete ring or shell-like appearance at wavelengths longer than $2 \mu\text{m}$ (see Figure 1 in Pandey et al. 2013). One can find a comprehensive review of this star-forming region in Reipurth (2008). The H II region associated with the S237 region (hereafter S237 H II region) is ionized by a star of spectral type B0.5 (Glushkov et al. 1975) or two B2 main-sequence-type stars (Pandey et al. 2013). Balser et al. (2011) estimated the velocity of ionized gas to be

about -0.64 km s^{-1} in the S237 H II region using a hydrogen radio recombination line (H87-93 α). Using CO ($J = 1-0$) line data, Yang et al. (2002) reported the radial velocity of molecular gas to be about -5.86 km s^{-1} toward IRAS 05281+3412. Leisawitz et al. (1989) studied the molecular gas content of 34 open star clusters, including S237, using ¹²CO (1-0) emission and suggested that a part of S237 is obscured by a molecular cloud. In the S237 region, Pandey et al. (2013) reported two separate stellar clusters and estimated a mean age of the young stellar objects (YSOs) to be 2 ± 1 Myr. Based on the morphology of the region, ages of the YSOs, and ionizing sources, they concluded that there is a triggered star formation process in the S237 region. Using the isochrone fitting in the Hertzsprung–Russell diagram, Lim et al. (2015) reported a median age of 2 Myr with a spread of 4.5 Myr for the age distribution of the pre-main-sequence (PMS) members in NGC 1931.

These previous studies suggest the presence of massive star (s) and ongoing star formation activity in the S237 region. The region is a relatively nearby star-forming site and has an interesting morphology, indicating that it is a promising site to explore the impact of ionizing star(s). Despite the availability of different observational data sets, the feedback of massive star(s) is not systematically studied in the S237 region. The physical conditions in the S237 region are yet to be determined, and the velocity structure of molecular gas is also unknown. Recently, *Herschel* observations have revealed that filaments are often seen in the star-forming regions (e.g., André et al. 2010; Molinari et al. 2010). However, the identification of dense clumps and filaments is still lacking in the S237 region. Furthermore, the star formation toward clumps and filaments in S237 is yet to be probed. A knowledge of the physical

environment of the region is very important for assessing the ongoing physical mechanisms. In the present paper, we study in detail the physical processes responsible for the interaction and feedback effect of massive star(s) on its surroundings. To understand the ongoing physical mechanisms in S237, we examine the distribution of dust temperature, column density, extinction, ionized emission, hot gas, neutral hydrogen gas, kinematics of molecular gas, and YSOs using the multi-wavelength data.

In Section 2, we describe the multiband data sets used in the present work. In Section 3, we provide the details of results obtained. In Section 4, we discuss the possible star formation scenario based on our findings. Finally, the results are summarized and concluded in Section 5.

2. DATA AND ANALYSIS

In the present work, we selected a region of $\sim 30'.6 \times 30'.6$ (central coordinates: $l = 173^\circ.993$; $b = 0^\circ.273$) around the S237 region. In the following, a brief description of the multiwavelength data from X-ray, optical $H\alpha$, near-infrared (NIR), and radio wavelengths is presented.

2.1. X-Ray Data

The *ROSAT* 0.5–2 keV X-ray image was obtained from the public archives (observation ID: WG931113P_N1_SI01.N1) maintained at the High Energy Astrophysics Science Archive Research Center (HEASARC) in the USA. The pixel scale of the image is $45''$. One can obtain more details about the *ROSAT* observations in Voges et al. (1999). A single *ROSAT* source (i.e., J053134.4+341242; Voges et al. 2000) is found in the S237 region. In the catalog, the total X-ray count was reported with an extraction radius of $300''$ (Voges et al. 1999), indicating the presence of an extended diffuse X-ray emission.

2.2. $H\alpha$ Narrowband Image

A narrowband $H\alpha$ image at $0.6563 \mu\text{m}$ was obtained from the Isaac Newton Telescope Photometric $H\alpha$ Survey of the Northern Galactic Plane (IPHAS; Drew et al. 2005) survey database. The survey was made using the Wide Field Camera (WFC) at the 2.5 m INT, located at La Palma. The WFC consists of four $4\text{k} \times 2\text{k}$ CCDs, in an L-shape configuration. The pixel scale is $0''.33$, and the instantaneous field is about 0.3 square degrees. One can find more details about the IPHAS survey in Drew et al. (2005).

2.3. NIR (1–5 μm) Data

NIR photometric *JHK* magnitudes of point sources have been obtained from the UKIDSS Galactic Plane Survey (GPS; Lawrence et al. 2007) sixth archival data release (UKIDSSDR6plus) and the Two Micron All Sky Survey (2MASS; Skrutskie et al. 2006). Note that the UKIDSS GPS data are not available for the entire selected region and are available only for the zone-I area as highlighted by a dotted line in Figure 1(b). Hence, 2MASS data are employed for the area where UKIDSS GPS observations are absent. The UKIDSS observations (resolution $\sim 0''.8$) were taken using the UKIRT Wide Field Camera (WFCAM; Casali et al. 2007). The UKIDSS GPS photometric data were calibrated using the 2MASS data. We obtained only reliable UKIDSS GPS

photometric data, following the conditions listed in Lucas et al. (2008) and Dewangan et al. (2015). 2MASS data were also retrieved for bright sources that were saturated in the GPS catalog. To obtain reliable 2MASS photometric data, only those sources from the 2MASS catalog that have photometric magnitude error of 0.1 and less in each band are chosen for the study.

Warm *Spitzer* IRAC 3.6 and $4.5 \mu\text{m}$ photometric images (resolution $\sim 2''$) and magnitudes of point sources have been retrieved from the Glimpse360⁵ (Whitney et al. 2011) survey. The photometric magnitudes were obtained from the GLIMPSE360 highly reliable catalog. To obtain further reliable Glimpse360 photometric data, only those sources are selected that have photometric magnitude error of 0.2 and less in each band.

2.4. Mid-infrared (12–22 μm) Data

We utilized the publicly available archival *WISE*⁶ (Wright et al. 2010) images at mid-infrared (MIR) $12 \mu\text{m}$ (spatial resolution $\sim 6''$) and $22 \mu\text{m}$ (spatial resolution $\sim 12''$). *WISE* photometric sensitivity⁷ is reported to be 0.86 and 5.4 mJy (11.3 and 8.0 Vega mag) at 12 and $22 \mu\text{m}$, respectively, in unconfused regions on the ecliptic plane. Saturation affects photometry for objects brighter than approximately 3.8 and -0.4 mag at 12 and $22 \mu\text{m}$, respectively.

2.5. Far-infrared and Submillimeter Data

Far-infrared (FIR) and submillimeter continuum images were downloaded from the *Herschel* Space Observatory data archives. The processed level2_5 images at $70 \mu\text{m}$, $160 \mu\text{m}$, $250 \mu\text{m}$, $350 \mu\text{m}$, and $500 \mu\text{m}$ were obtained using the *Herschel* Interactive Processing Environment (HIPE; Ott 2010). The beam sizes of the *Herschel* images at $70 \mu\text{m}$, $160 \mu\text{m}$, $250 \mu\text{m}$, $350 \mu\text{m}$, and $500 \mu\text{m}$ are $5''.8$, $12''$, $18''$, $25''$, and $37''$, respectively (Griffin et al. 2010; Poglitsch et al. 2010). In this work, *Herschel* continuum images are utilized to compute the *Herschel* temperature and column density maps of the S237 region. Following the method described in Mallick et al. (2015), we obtained the *Herschel* temperature and column density maps from a pixel-by-pixel spectral energy distribution (SED) fit with a modified blackbody to the cold dust emission in the *Herschel* 160–500 μm wavelengths (also see Dewangan et al. 2015). The *Herschel* $70 \mu\text{m}$ data are not used in the analysis, because the $70 \mu\text{m}$ emission is dominated by the UV-heated warm dust. In the following, a brief step-by-step description of the procedures is described.

The *Herschel* $160 \mu\text{m}$ image is calibrated in the units of Jy pixel^{-1} , while the images at 250–500 μm are calibrated in the surface brightness units of MJy sr^{-1} . The plate scales of the $160 \mu\text{m}$, $250 \mu\text{m}$, $350 \mu\text{m}$, and $500 \mu\text{m}$ images are $3''.2$, $6''$, $10''$, and $14'' \text{ pixel}^{-1}$, respectively. In the first step, prior to the SED fit, the $160 \mu\text{m}$, $250 \mu\text{m}$, and $350 \mu\text{m}$ images were convolved to the lowest angular resolution of the $500 \mu\text{m}$ image ($\sim 37''$) and were converted into the same flux units (i.e., Jy pixel^{-1}). Furthermore, these images were regridded to the pixel size of the $500 \mu\text{m}$ image ($\sim 14''$). These steps were carried out using the convolution kernels available in the HIPE software. Next,

⁵ <http://www.astro.wisc.edu/sirtf/glimpse360/>

⁶ *Wide-field Infrared Survey Explorer*, which is a joint project of the University of California and the JPL, Caltech, funded by NASA.

⁷ <http://wise2.ipac.caltech.edu/docs/release/allsky/>

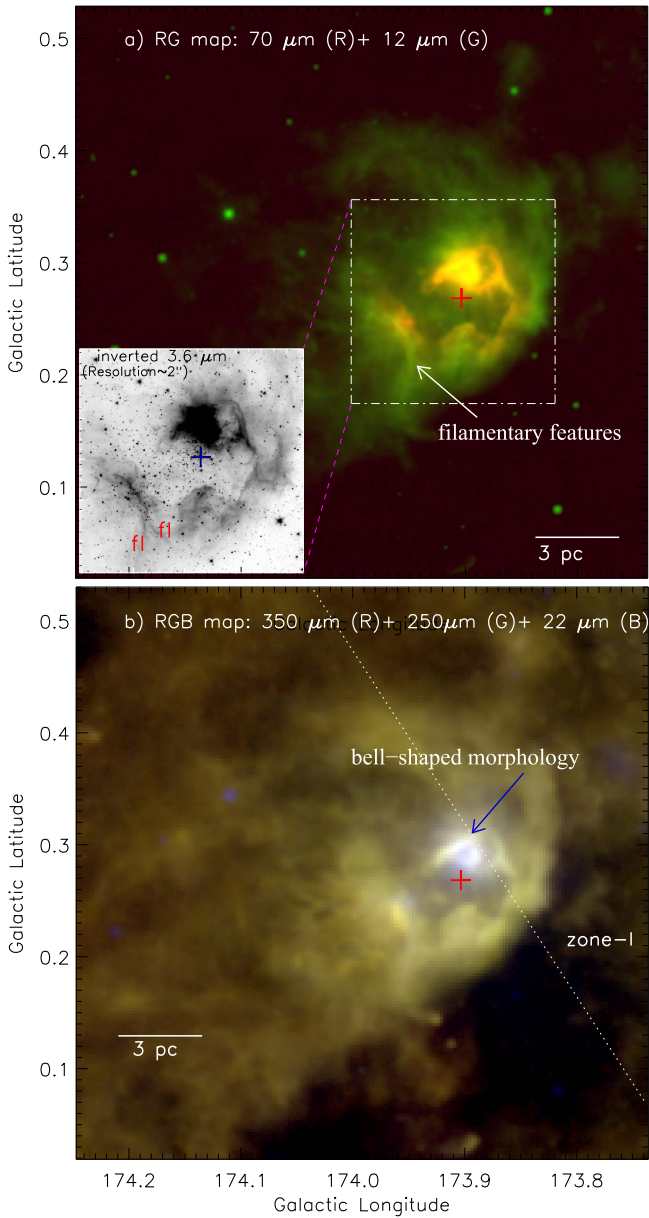


Figure 1. Distribution of the MIR and submillimeter emissions toward the S237 region (size of the selected region $\sim 30'6 \times 30'6$ (~ 20.5 pc \times 20.5 pc at a distance of 2.3 kpc); centered at $l = 173^{\circ}993$; $b = 0^{\circ}273$). (a) Two-color composite image (in logarithmic gray scale), which clearly illustrates the morphology of the region. The inset on the bottom left shows the central region in zoomed-in view, using the *Spitzer* 3.6 μm image (inverted gray scale; see the dot-dashed white box). Two filamentary features are highlighted by labels “fl.” (b) Composite trichromatic image of the S237 region with the *Herschel* 350 μm and 250 μm and *WISE* 22 μm bands in red, green, and blue, respectively. The UKIDSS GPS data are available only for the zone-I area as highlighted by a dotted line. In both panels, the position of IRAS 05281+3412 is marked by a plus sign. In both panels, the scale bar corresponding to 3 pc (at a distance of 2.3 kpc) is shown in the bottom left. The panels reveal a shell-like morphology of the region, filamentary features, and a bell-shaped cavity-like structure.

the sky background flux level was determined to be 0.051, 0.115, 0.182, and -0.0009 Jy pixel $^{-1}$ for the 500 μm , 350 μm , 250 μm , and 160 μm images (size of the selected region $\sim 5'6 \times 7'8$; centered at $l = 174^{\circ}127$, $b = -0^{\circ}222$), respectively. To avoid diffuse emission associated with the selected target, the featureless dark area away from the S237 region was carefully chosen for the background estimation.

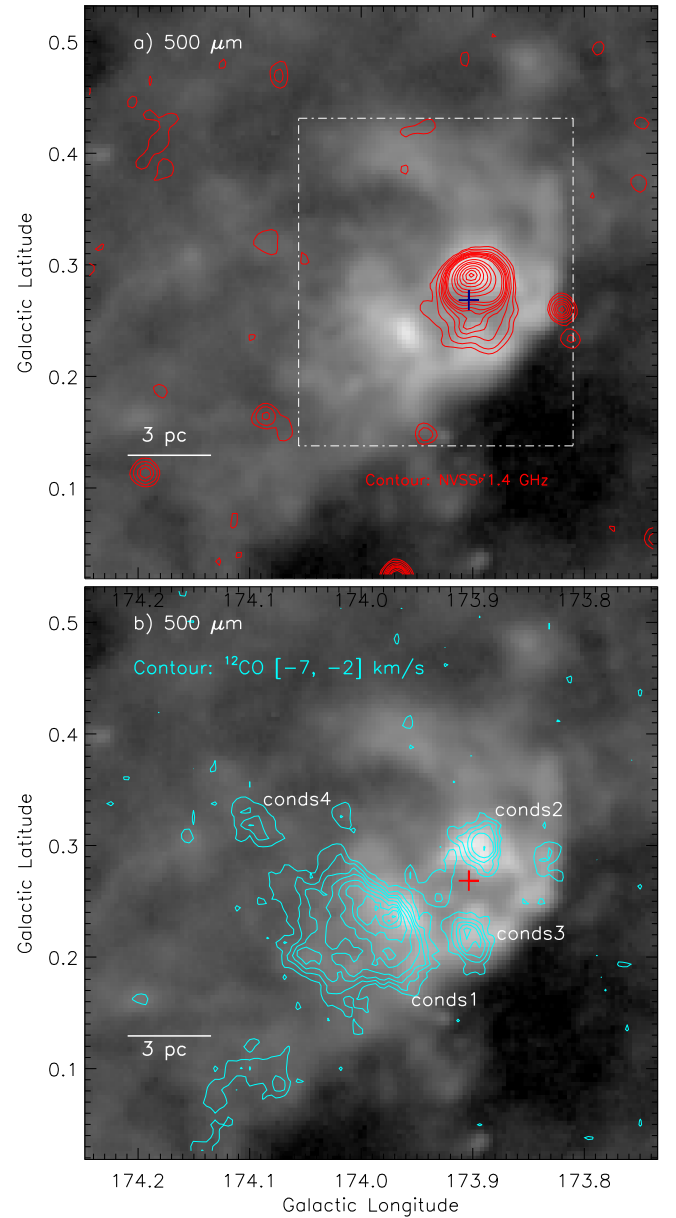


Figure 2. Distribution of the submillimeter, ionized, and molecular emissions toward the S237 region. (a) The radio continuum contours from the NVSS at 1.4 GHz are overlaid on the *Herschel* 500 μm image. The NVSS contours are superimposed with levels of 0.5%, 1%, 2%, 3%, 4%, 5%, 6%, 8%, 10%, 20%, 30%, 40%, 55%, 70%, 85%, and 95% of the peak value (i.e., 0.1936 Jy beam $^{-1}$). The dot-dashed white box encompasses the area shown in Figure 3(a). (b) The integrated ^{12}CO (1–0) emission contours are overplotted on the *Herschel* 500 μm image. The ^{12}CO emission contours are superimposed with levels of 1%, 2%, 3%, 4%, 55%, 70%, 80%, 90%, and 99% of the peak value (i.e., 36.5639 K km s $^{-1}$). In each panel, the scale bar at the bottom left corner corresponds to 3 pc (at a distance of 2.3 kpc). In each panel, the marked symbol is similar to those shown in Figure 1. The panels show the distribution of ionized emission, molecular gas, and dense materials in the region.

Finally, to obtain the maps, we fitted the observed flux densities at each pixel with the modified blackbody model (see Equations (8) and (9) in Mallick et al. 2015). The fitting was done using the four data points for each pixel, retaining the dust temperature (T_d) and the column density ($N(\text{H}_2)$) as free parameters. In the analysis, we adopted a mean molecular weight per hydrogen molecule $\mu_{\text{H}_2} = 2.8$ (Kauffmann et al. 2008) and an absorption coefficient $\kappa_\nu = 0.1(\nu/1000 \text{ GHz})^\beta \text{ cm}^2 \text{ g}^{-1}$, including a gas-to-dust

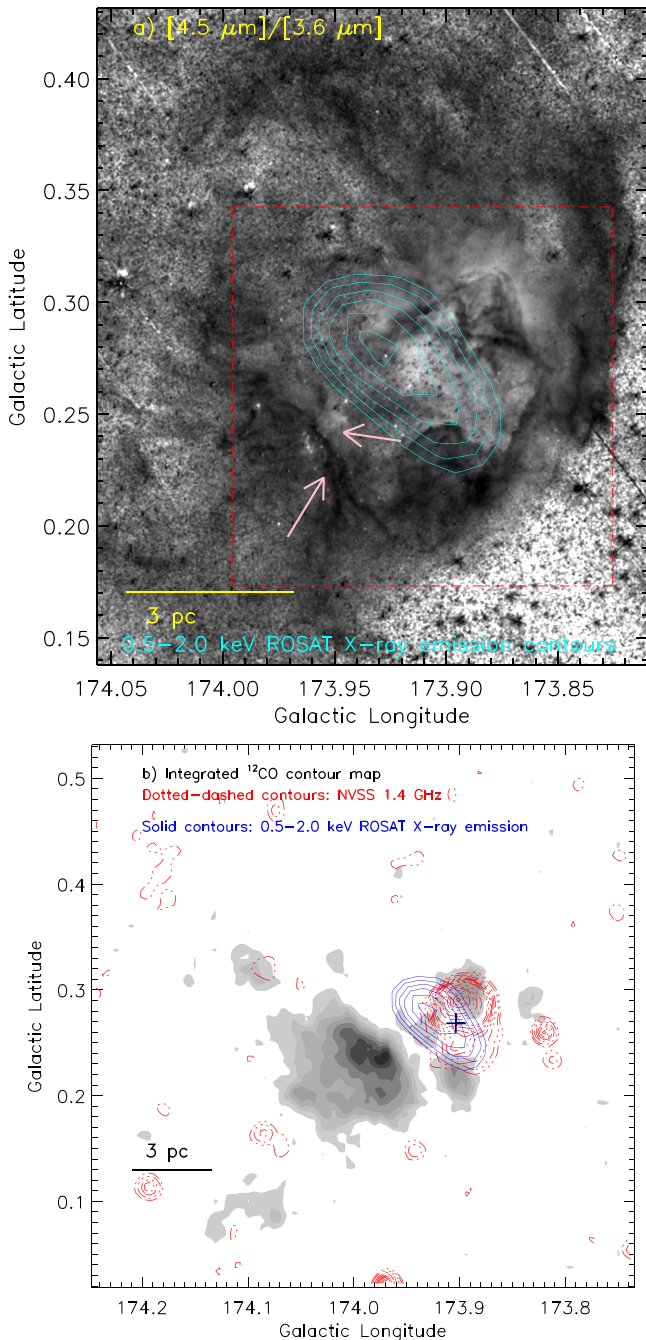


Figure 3. (a) *Spitzer* ratio map of $4.5 \mu\text{m}/3.6 \mu\text{m}$ emission. The ratio map is subjected to median filtering with a width of 5 pixels and smoothed by 4 pixels \times 4 pixels using a boxcar algorithm. The dot-dashed box (in red) encompasses the area shown in Figure 4. The $4.5 \mu\text{m}/3.6 \mu\text{m}$ emission contour (gray dot-dashed contour) is also shown on the image with a representative value of 0.75, tracing the shell-like morphology. (b) Contour map of integrated ^{12}CO emission in the velocity range of -7 to -2 km s^{-1} . The contour levels are similar to the one shown in Figure 2(b). The NVSS contours (red dot-dashed contours) are also superimposed with similar levels to that shown in Figure 2(a). The $0.5\text{--}2.0 \text{ keV ROSAT X-ray emission contours}$ (solid contours) of S237 are overplotted on both panels. The X-ray image is Gaussian smoothed with a radius of 3 pixels. In both panels, the scale bar at the bottom left corner corresponds to 3 pc (at a distance of 2.3 kpc).

ratio $R_t = 100$, with a dust spectral index of $\beta = 2$ (see Hildebrand 1983). The final *Herschel* temperature and column density maps are presented in Section 3.3.

2.6. Molecular CO Line Data

The observations of $^{12}\text{CO}(1\text{--}0)$ and $^{13}\text{CO}(1\text{--}0)$ emission were taken using the Five College Radio Astronomy Observatory (FCRAO) 14 m telescope in New Salem, Massachusetts. The FCRAO beam sizes are $45''$ (with angular sampling of $22''/5$) and $46''$ (with angular sampling of $22''/5$) for ^{12}CO and ^{13}CO , respectively. Both sets of line data have a velocity resolution of 0.25 km s^{-1} . Typical rms values for the spectra are 0.25 K for ^{12}CO and 0.2 K for ^{13}CO (e.g., Heyer et al. 1996). The S237 region was observed as part of the Extended Outer Galaxy Survey (E-OGS; Brunt 2004), which extends the coverage of the FCRAO Outer Galaxy Survey (OGS; Heyer et al. 1998) to Galactic longitude $l = 193^\circ$, over a Galactic latitude range of $-3^\circ.5 \leq b \leq +5^\circ.5$. These ^{12}CO and ^{13}CO data cubes were provided by M. Heyer and C. Brunt (private communication). The FCRAO ^{12}CO profile along the line of sight to the S237 region shows a single velocity component at $v = -4.6 \text{ km s}^{-1}$.

2.7. Radio Continuum Data

A radio continuum map at 1.4 GHz was retrieved from the NRAO VLA Sky Survey (NVSS) archive. The survey covers the sky north of $\delta_{2000} = -40^\circ$ at 1.4 GHz with a beam of $45''$ and a nearly uniform sensitivity of $\sim 0.45 \text{ mJy beam}^{-1}$ (Condon et al. 1998).

2.8. HI Line Data

The 21 cm HI line data were obtained from the Canadian Galactic Plane Survey (CGPS; Taylor et al. 2003). The velocity resolution of HI line data is 1.32 km s^{-1} , sampled every 0.82 km s^{-1} . The data have a spatial resolution of $1' \times 1' \text{ csc}\delta$. The line data have a brightness temperature sensitivity of $\Delta T_B = 3.5 \sin\delta \text{ K}$. One can find more details about the CGPS observing and data processing strategy in Taylor et al. (2003).

3. RESULTS

3.1. Multiband Picture of S237

3.1.1. Continuum Emission and Gas Distribution in S237

The longer-wavelength data enable us to penetrate deeper into the star-forming cloud despite the high extinction, allowing us to infer the physical environment of a given star-forming region. In this section, we employ multiband data to trace the physical structure of the S237 region. Figure 1(a) shows a two-color composite image using *Herschel* $70 \mu\text{m}$ in red and *WISE* $12.0 \mu\text{m}$ in green. A three-color composite image ($350 \mu\text{m}$ [red], $250 \mu\text{m}$ [green], and $22 \mu\text{m}$ [blue]) is shown in Figure 1(b). The *Herschel* and *WISE* images depict a broken or incomplete ring or shell-like appearance of the S237 region at wavelengths longer than $2 \mu\text{m}$. The images reveal a prominent bell-shaped cavity-like morphology and elongated filamentary features at the center and the edge of the shell-like structure, respectively (see Figures 1(a) and (b)). The inset on the bottom left shows the zoomed-in view around IRAS 05281+3412 using the *Spitzer* $3.6 \mu\text{m}$ image (see Figure 1(a)). The filamentary features are also highlighted in the image. Figure 2 shows the radio continuum and molecular emissions overlaid on the *Herschel* image at $500 \mu\text{m}$. The bulk of the $160\text{--}500 \mu\text{m}$ emission comes from cold dust components (see Section 3.3 for quantitative estimates), while the emission at $22 \mu\text{m}$ traces the

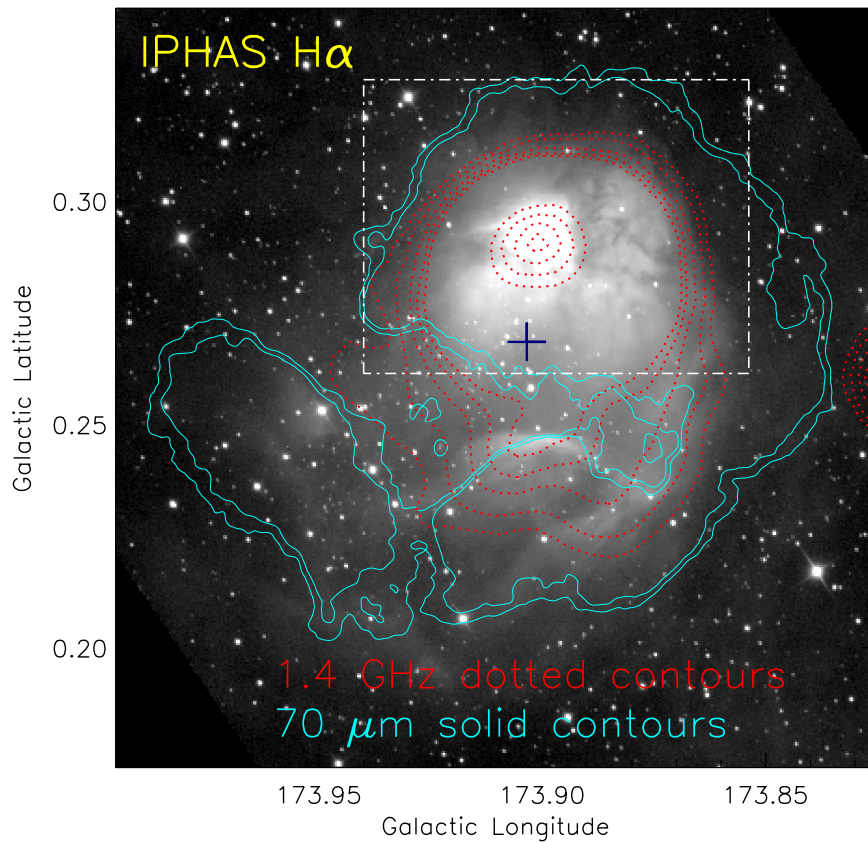


Figure 4. IPHAS $H\alpha$ grayscale image overlaid with the NVSS 1.4 GHz and *Herschel* 70 μm emission contours. The NVSS 1.4 GHz dotted contours (in red) are shown with levels of 0.5%, 1%, 2%, 3%, 4%, 55%, 70%, 85%, and 95% of the peak value (i.e., 0.1936 Jy beam $^{-1}$). The dot-dashed white box encompasses the area shown in Figures 5(a) and (b).

warm dust emission (see Figure 1(b)). In Figure 2(a), we show the spatial distribution of ionized emission traced in the NVSS 1.4 GHz map, concentrating near the bell-shaped cavity-like morphology. This also implies that the ionized emission is located within the shell-like structure. The radio continuum emission is absent toward the elongated filamentary features. In Figure 2(b), we present the molecular ^{12}CO ($J = 1-0$) gas emission in the direction of the S237 region, revealing at least four molecular condensations (designated as conds1–4). The ^{12}CO profile traces the region in a velocity range between -7 and -2 km s $^{-1}$. The molecular condensations are also found toward the filamentary features and the bell-shaped cavity-like morphology. It can be seen that the majority of molecular gas is distributed toward the molecular condensation conds1, where filamentary features are observed. The details of the integrated ^{12}CO map, as well as kinematics of molecular gas, are described in Section 3.4.

Together, Figures 1 and 2 have allowed us to obtain a pictorial multiwavelength view of the environment in the S237 region.

3.1.2. Lyman Continuum Flux

In this section, we estimate the number of Lyman continuum photons using the radio continuum map, which will allow us to derive the spectral type of the powering candidate associated with the S237 H II region. In Figure 2(a), the NVSS radio map traces a spherical morphology of the S237 H II region. We used the clumpfind IDL program (Williams et al. 1994) to estimate the integrated flux density, and the radio continuum flux was

integrated up to the 0.3% contour level of peak intensity. Using the 1.4 GHz map, we computed the integrated flux density (S_ν) and radius ($R_{\text{H II}}$) of the H II region to be 708 mJy and 1.27 pc, respectively. The integrated flux density allows us to compute the number of Lyman continuum photons (N_{uv}), using the following equation (Matsakis et al. 1976):

$$N_{\text{uv}}(s^{-1}) = 7.5 \times 10^{46} \left(\frac{S_\nu}{\text{Jy}} \right) \left(\frac{D}{\text{kpc}} \right)^2 \left(\frac{T_e}{10^4 \text{K}} \right)^{-0.45} \times \left(\frac{\nu}{\text{GHz}} \right)^{0.1}, \quad (1)$$

where S_ν is the measured total flux density in Jy, D is the distance in kpc, T_e is the electron temperature, and ν is the frequency in GHz. This analysis is performed for an electron temperature of 10,000 K and a distance of 2.3 kpc. We obtain an N_{uv} (or $\log N_{\text{uv}}$) of $\sim 2.9 \times 10^{47}$ s $^{-1}$ (47.47) for the S237 H II region, which corresponds to a single ionizing star of spectral type B0.5V–B0V (see Table II in Panagia 1973 for a theoretical value).

The knowledge of N_{uv} and $R_{\text{H II}}$ values is also used to infer the dynamical age (t_{dyn}) of the S237 H II region. The age of the H II region can be computed at a given radius $R_{\text{H II}}$, using the following equation (Dyson & Williams 1980, p. 204):

$$t_{\text{dyn}} = \left(\frac{4 R_s}{7 c_s} \right) \left[\left(\frac{R_{\text{H II}}}{R_s} \right)^{7/4} - 1 \right] \quad (2)$$

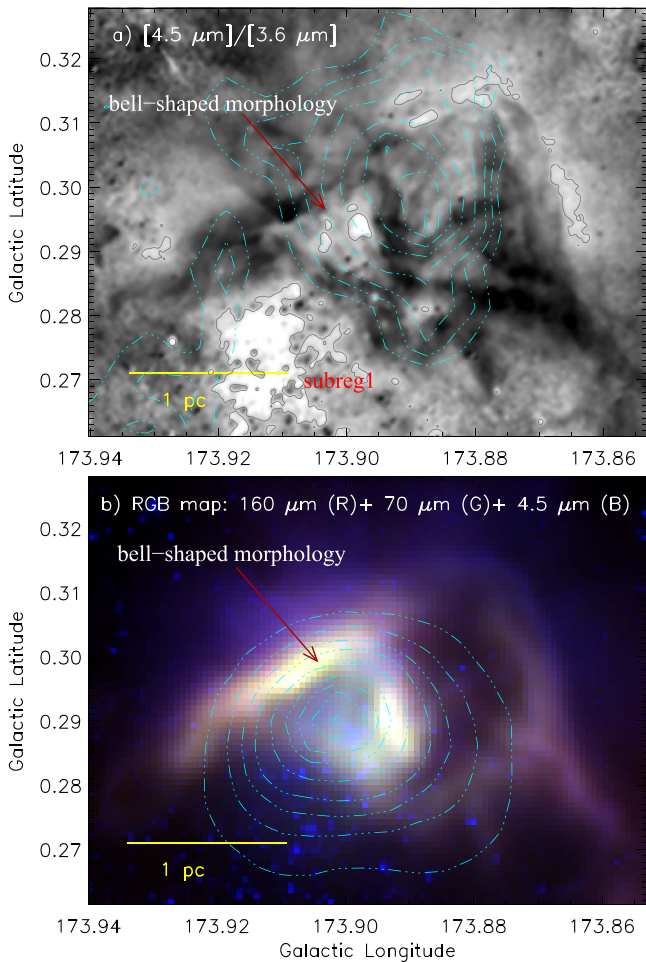


Figure 5. (a) *Spitzer* ratio map of $4.5 \mu\text{m}/3.6 \mu\text{m}$ emission overlaid with the integrated ^{12}CO ($J = 1-0$) contours. The ^{12}CO contours are shown with levels of 20%, 30%, 40%, 55%, 70%, 80%, 90%, and 99% of the peak value (i.e., $20.076 \text{ K km s}^{-1}$). The $4.5 \mu\text{m}/3.6 \mu\text{m}$ emission contour (in dark gray) is also shown on the image with a representative value of 0.99. (b) Color composite map using $160 \mu\text{m}$ (red), $70 \mu\text{m}$ (green), and $4.5 \mu\text{m}$ (blue) images. The map is overlaid with the NVSS 1.4 GHz contours. The NVSS 1.4 GHz contours are shown with levels of 10%, 20%, 30%, 40%, 55%, 70%, 80%, 90%, and 99% of the peak value (i.e., $0.1936 \text{ Jy beam}^{-1}$). In each panel, the scale bar at the bottom left corner corresponds to 1 pc (at a distance of 2.3 kpc).

where c_s is the isothermal sound velocity in the ionized gas ($c_s = 11 \text{ km s}^{-1}$; Bisbas et al. 2009), $R_{\text{H II}}$ is previously defined, and R_s is the radius of the Strömgren sphere ($= (3N_{\text{uv}}/4\pi n_0^2 \alpha_B)^{1/3}$, where the radiative recombination coefficient $\alpha_B = 2.6 \times 10^{-13} (10^4 \text{ K/T})^{0.7} \text{ cm}^3 \text{ s}^{-1}$ Kwan 1997, N_{uv} is defined earlier, and “ n_0 ” is the initial particle number density of the ambient neutral gas). Assuming a typical value of n_0 (such as 10^3 [10^4] cm^{-3}), we calculated the dynamical age of the S237 H II region to be ~ 0.2 (0.8) Myr.

3.2. IRAC Ratio Map and H I Gas

To infer the signatures of molecular outflows and the impact of massive stars on their surroundings, the *Spitzer* IRAC ratio maps have been employed in combination with the radio continuum emission (Povich et al. 2007; Watson et al. 2008; Dewangan & Anandarao 2011; Dewangan et al. 2012, 2016). Due to almost identical point response functions (PRFs) of IRAC $3.6 \mu\text{m}$ and $4.5 \mu\text{m}$ images, a ratio map of $4.5 \mu\text{m}/$

$3.6 \mu\text{m}$ emission can be obtained directly using the ratio of $4.5 \mu\text{m}$ to $3.6 \mu\text{m}$ images. IRAC $4.5 \mu\text{m}$ band harbors a hydrogen recombination line $\text{Br}\alpha$ ($4.05 \mu\text{m}$) and a prominent molecular hydrogen line emission ($\nu = 0-0 \text{ S}(9)$; $4.693 \mu\text{m}$), which can be excited by outflow shocks. IRAC $3.6 \mu\text{m}$ band contains polycyclic aromatic hydrocarbon (PAH) emission at $3.3 \mu\text{m}$, as well as a prominent molecular hydrogen feature at $3.234 \mu\text{m}$ ($\nu = 1-0 \text{ O}(5)$). The ratio map of $4.5 \mu\text{m}/3.6 \mu\text{m}$ emission is shown in Figure 3(a), tracing the bright and dark/black regions. The shell-like morphology is depicted, and the map traces the edges of the shell (see dark/black regions in Figure 3(a)). The $0.5-2 \text{ keV}$ X-ray emission is detected within the shell-like morphology, indicating the presence of hot gas emission in the region (see Figure 3(a)). The prominent bell-shaped cavity and the elongated filamentary features are also seen in the ratio map (see arrows and highlighted dot-dashed box in Figure 3(a)). In Figure 3(b), the distribution of molecular gas, ionized gas, and hot gas emission is shown together. In the ratio $4.5 \mu\text{m}/3.6 \mu\text{m}$ map, the bright emission regions suggest the domination of $4.5 \mu\text{m}$ emission, while the black or dark gray regions indicate the excess of $3.6 \mu\text{m}$ emission. In Figure 4, we present the $\text{H}\alpha$ image overlaid with the NVSS 1.4 GHz and *Herschel* $70 \mu\text{m}$ emission. The $\text{H}\alpha$ image shows the extended diffuse $\text{H}\alpha$ emission in the S237 region, which is well distributed within the shell-like morphology. Figure 4 also shows the spatial match between the $\text{H}\alpha$ emission and the radio continuum emission. Figures 5(a) and (b) show a zoomed-in ratio map and color composite image toward the radio peak. A bell-shaped cavity is evident, and the peaks of radio continuum 1.4 GHz emission and diffuse $\text{H}\alpha$ emission are present within it (see Figures 4 and 5(b)). The warm dust emission traced in the $70 \mu\text{m}$ image depicts the walls of the bell-shaped cavity (see Figure 5(b)). However, the peak of molecular $^{12}\text{CO}(1-0)$ emission does not coincide with the radio continuum peak (see Figure 5). This indicates that the bell-shaped cavity can originate from the impact of ionized emission (also see Section 3.6). In the ratio map, there are bright emission regions near the radio continuum emission, indicating the excess of $4.5 \mu\text{m}$ emission. As mentioned above, the $4.5 \mu\text{m}$ band contains the $\text{Br}\alpha$ feature at $4.05 \mu\text{m}$. Hence, due to the presence of ionized emission, these bright emission regions probably trace the $\text{Br}\alpha$ features. In Figure 5(a), the excess of $4.5 \mu\text{m}$ emission is also observed to the bottom of the bell-shaped morphology, which is designated as subreg1 and is coincident with the $0.5-2 \text{ keV}$ X-ray peak emission. We also find a bright emission region near the elongated filamentary features where the radio continuum emission is absent (see arrows in Figure 3(a)). Hence, this emission is probably tracing the outflow activities. Considering the presence of the $3.3 \mu\text{m}$ PAH feature in the $3.6 \mu\text{m}$ band, the edges of the shell-like morphology around the H II region appear to depict photo-dissociation regions (or photon-dominated regions, PDRs).

In Figure 6, we present 21 cm H I velocity channel maps of the S237 region. The bright H I feature is seen near the 1.4 GHz emission; however, the sphere-like shell morphology is depicted in black or dark gray regions. It appears that the black or dark gray regions in the H I channel maps trace the H I self-absorption (HISA) features (i.e., shell-like HISA features; e.g., Kerton 2005). It has been suggested that the HISA features are produced by the residual amounts of very cold H I gas in molecular clouds (Burton et al. 1978; Baker & Burton 1979; Burton & Liszt 1981; Liszt et al. 1981). In the S237 region, the

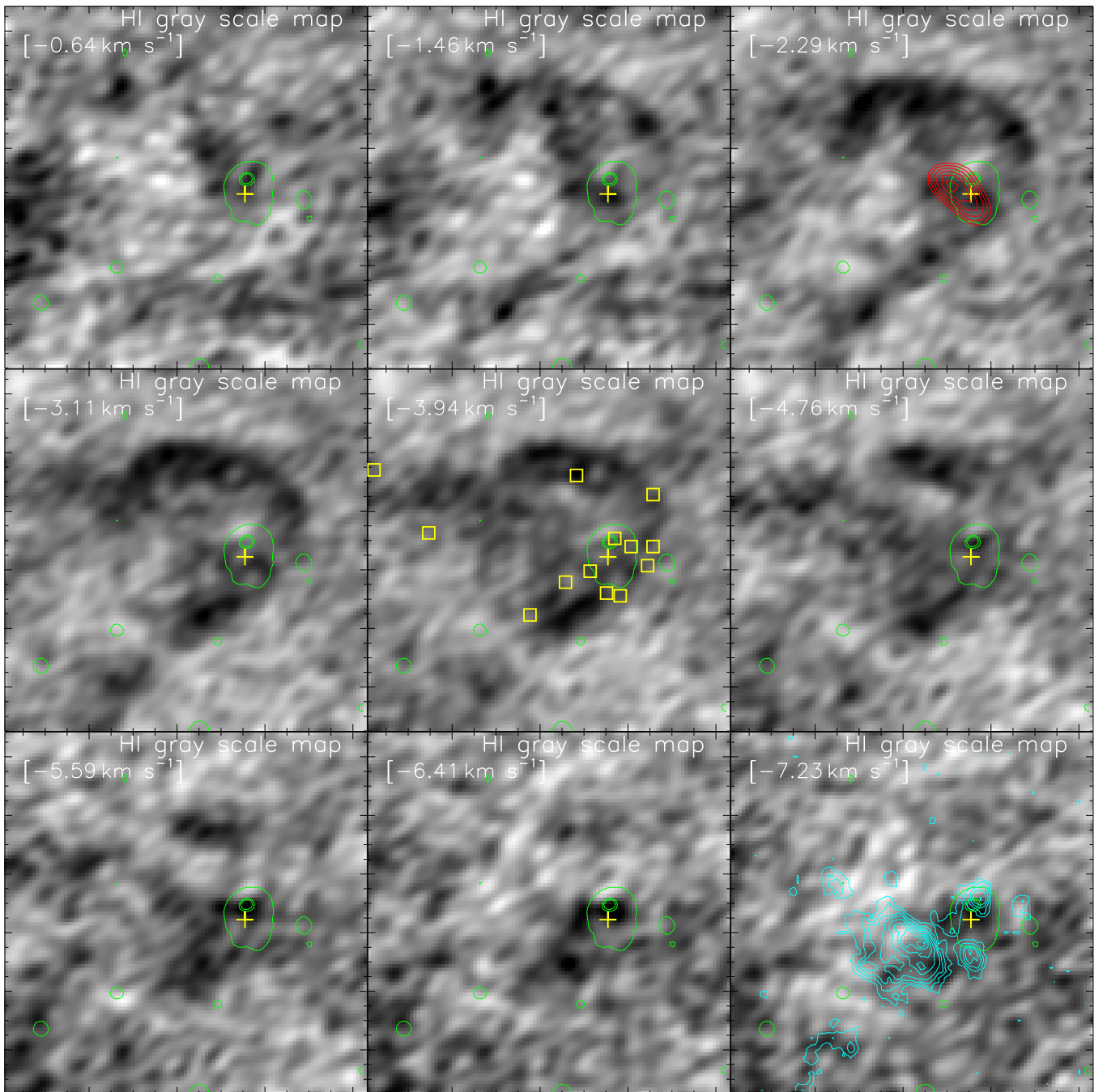


Figure 6. CGPS 21 cm H I velocity channel maps of the S237 region. The velocity value (in km s^{-1}) is labeled in each panel. In each panel, the NVSS 1.4 GHz contours (in green) are superimposed with levels of 1%, 55%, and 70% of the peak value (i.e., $0.1936 \text{ Jy beam}^{-1}$), tracing the ionized hydrogen emission. In each panel, the position of IRAS 05281+3412 is marked by a plus sign. In the third panel (at -2.29 km s^{-1}), the 0.5–2.0 keV *ROSAT* X-ray emission contours (red dot-dashed contours) are similar to the one shown in Figure 3(a). In the fifth panel (at -3.94 km s^{-1}), the identified *Herschel* clumps are marked by squares (in yellow; also see Figure 8(b)). To enhance the H I features, each channel map is smoothed with a boxcar average of 3 pixels in width. In the last panel, the ^{12}CO emission contours are similar to the one shown in Figure 2(b). In the maps, the sphere-like shell morphology of the S237 region is revealed as H I self-absorption features (i.e., cold H I traced in absorption against warmer background H I; Kerton 2005).

HISA features are more prominent in a velocity range of -2.29 to -3.11 km s^{-1} . The 21 cm H I line data are presented here only for a morphological comparison with the infrared images. The 0.5–2 keV X-ray emission is also shown in a channel map (at -2.29 km s^{-1}), allowing us to infer the distribution of cold H I gas and hot gas emission in the region. In Figure 7, to compare the morphology of the S237 region, we have shown infrared images (at $22 \mu\text{m}$ and $250 \mu\text{m}$) and an H I map (at 21 cm). We find that the shell-like HISA feature is spatially

correlated with dust emission as traced in the *Spitzer*, *WISE*, and *Herschel* images. The presence of H I further indicates the PDRs surrounding the H II region and hot gas emission.

3.3. *Herschel* Temperature and Column Density Maps

The *Herschel* temperature and column density maps are used to infer the physical conditions present in a given star-forming region. In Figure 8, we show the final temperature and column

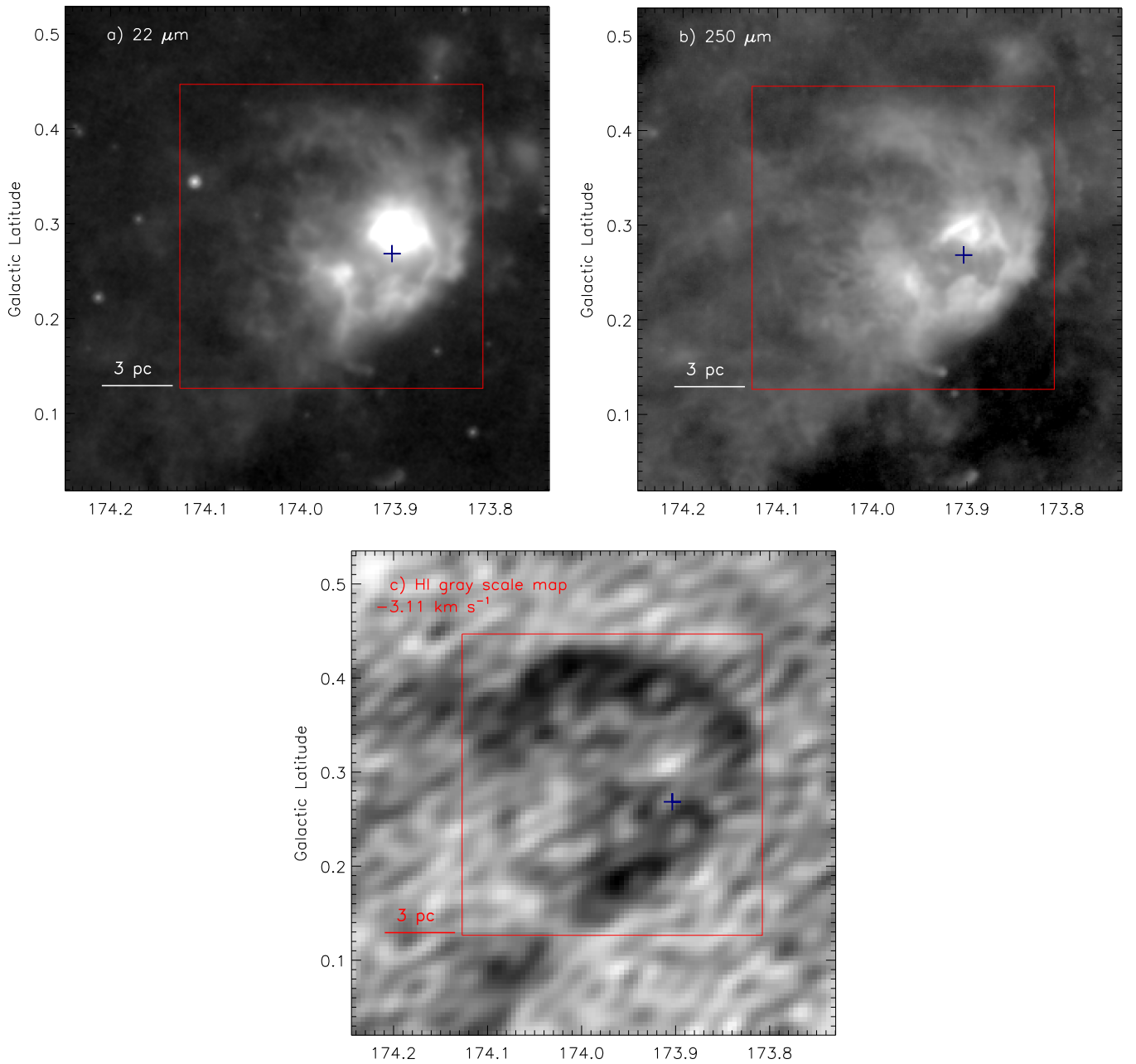


Figure 7. Comparison of infrared images and HI map (at -3.11 km s^{-1}) of the S237 region. In each panel, a solid box (in red) shows an area where the shell-like morphology of the region is seen. In each panel, the scale bar at the bottom left corner corresponds to 3 pc (at a distance of 2.3 kpc).

density maps (resolution $\sim 37''$). The procedures for calculating the *Herschel* temperature and column density maps were mentioned in Section 2.5.

In the *Herschel* temperature map, the area near the H II region is traced with the considerably warmer gas ($T_d \sim 29\text{--}47 \text{ K}$; see Figure 8(a)). The *Herschel* temperature map traces the edges of the shell in a temperature range of about 22–28 K. Several condensations are found in the column density map, and one of the condensations (see clump1) has the highest column density (peak $N(\text{H}_2) \sim 3.6 \times 10^{21} \text{ cm}^{-2}$; $A_V \sim 3.8 \text{ mag}$) located toward the filamentary features (see Figure 8(b)). The relation between optical extinction and hydrogen column density ($A_V = 1.07 \times 10^{-21} N(\text{H}_2)$; Bohlin et al. 1978) is used here. Krumholz & McKee (2008) proposed a threshold value of 1 g cm^{-2} (or corresponding column densities of $\sim 3 \times 10^{23} \text{ cm}^{-2}$) for formation of massive stars.

This implies that the formation of massive stars in the identified *Herschel* clumps is unlikely. The column density structure of S237 appears nonhomogeneous, with higher column density clumps engulfed in a medium with lower column density. The bell-shaped cavity is also seen in the column density map.

In the column density map, we employed the clumpfind algorithm to identify the clumps and their total column densities. We find 13 clumps, which are labeled in Figure 8 (b), and their boundaries are also shown in Figure 8(c). Out of the 13 clumps, 7 (e.g., clumps 1, 3, 4, 6, 7, 9, and 13) are found toward the edges of the shell-like structure, while three other clumps (e.g., clumps 2, 5, and 11) are located within the shell-like structure and the remaining three clumps (e.g., clumps 8, 10, and 12) are away from the shell-like structure. To assess the spatial distribution of clumps with respect to the HISA features, these clumps are also marked in the CGPS 21 cm HI single-

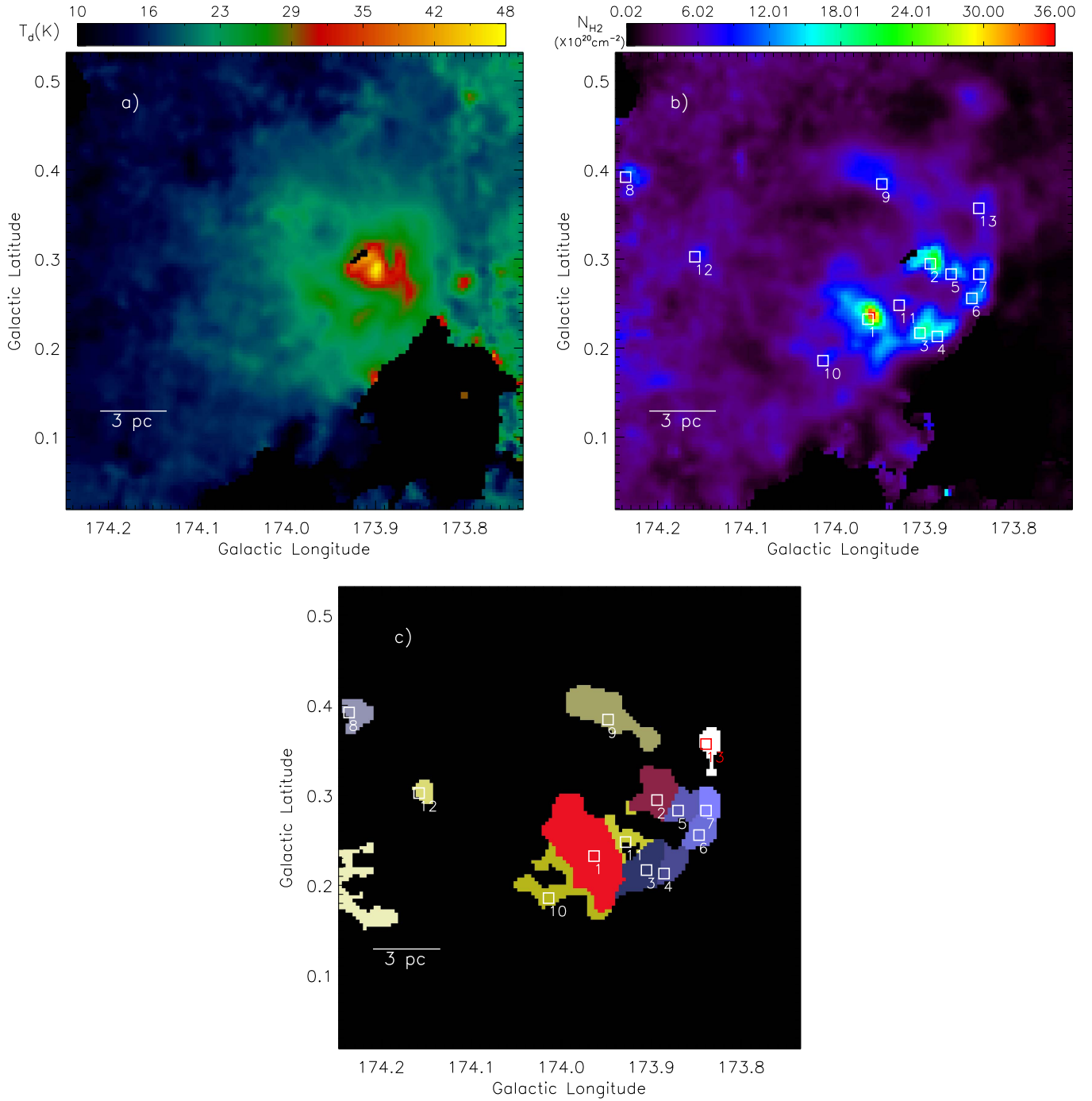


Figure 8. *Herschel* (a) temperature map and (b) column density ($N(\text{H}_2)$) map of the region (see text for details). The column density map allows us to infer the extinction with $A_V = 1.07 \times 10^{-21} N(\text{H}_2)$ and to identify the clumps (see text for details). The identified clumps are marked by squares, and the boundary of each identified clump is shown in Figure 8(c) (also see Table 1). (c) The boundary of each identified clump is highlighted along with its corresponding clump ID (see Table 1 and also Figure 8(b)). In each panel, the scale bar at the bottom left corner corresponds to 3 pc (at a distance of 2.3 kpc).

channel map at -3.94 km s^{-1} (see Figure 6). The mass of each clump is computed using its total column density and can be determined using the formula

$$M_{\text{clump}} = \mu_{\text{H}_2} m_{\text{H}} \text{Area}_{\text{pix}} \Sigma N(\text{H}_2) \quad (3)$$

where μ_{H_2} is assumed to be 2.8, Area_{pix} is the area subtended by 1 pixel, and $\Sigma N(\text{H}_2)$ is the total column density. The mass of each *Herschel* clump is tabulated in Table 1. The table also contains an effective radius of each clump, which is provided by the clumpfind algorithm. The clump masses vary between

10 and $260 M_{\odot}$. The most massive clump (i.e., clump1) associated with the molecular condensation *conds1* (see Figure 2(b)) is away from the radio peak, while clump2, linked to the molecular condensation *conds2* (see Figure 2(b)), is associated with the H II region.

3.4. Kinematics of Molecular Gas

In this section, we present distributions of ^{12}CO ($J = 1-0$) and ^{13}CO ($J = 1-0$) gas in the S237 region. An inspection of

Table 1
Summary of the Properties of the *Herschel* Clumps Identified in the S237 Region (see Figures 8(b) and (c))

ID	l (deg)	b (deg)	R_c (pc)	M_{clump} (M_{\odot})
1	173.9637	0.2325	1.8	258.6
2	173.8937	0.2947	1.0	84.3
3	173.9054	0.2169	1.0	80.2
4	173.8860	0.2130	0.7	37.4
5	173.8704	0.2830	0.7	35.2
6	173.8471	0.2558	0.7	36.0
7	173.8393	0.2830	0.6	25.0
8	174.2360	0.3919	0.7	27.6
9	173.9482	0.3842	1.3	85.7
10	174.0143	0.1858	1.1	60.4
11	173.9287	0.2480	0.7	24.1
12	174.1582	0.3025	0.5	11.7
13	173.8393	0.3569	0.6	18.5

Note. Column (1) lists the IDs given to the clump. The table also contains positions, deconvolved effective radius (R_c), and clump mass (M_{clump}).

the ^{12}CO and ^{13}CO line profiles reveals that the molecular cloud associated with the S237 region (i.e., S237 molecular cloud) is well traced in a velocity range of -7 to -2 km s^{-1} . In general, ^{12}CO emission is optically thicker than ^{13}CO . To study the spatial distribution of the molecular gas in the S237 region, in Figure 9 we present ^{12}CO ($J = 1-0$) velocity channel maps at different velocities within the velocity range from -6.25 to -1.75 km s^{-1} in steps of 0.5 km s^{-1} . The channel maps show at least four molecular condensations (i.e., conds1–4), and the bulk of the molecular gas is found toward the condensation “conds1.” In Figure 10, we show the ^{13}CO ($J = 1-0$) velocity channel maps as a zoomed-in view toward the condensation “conds1,” where the high- and low-velocity gas distribution is evident toward the *Herschel* clump1. Note that the molecular condensation “conds1” contains the elongated filamentary features and a massive *Herschel* clump (i.e., clump1). In Figure 11, we present the integrated ^{12}CO and ^{13}CO intensity maps and the galactic position–velocity maps. In the position–velocity diagrams of the ^{12}CO emission, we find a noticeable velocity gradient along the condensation “conds1” (see Figures 11(c) and (e)) and an almost inverted C-like structure (see Figure 11(e)). In Figure 11 (see right panels), we also show the integrated ^{13}CO ($1-0$) intensity map and the position–velocity maps. The optical depth in ^{13}CO is much lower than that in ^{12}CO , and the ^{13}CO data can trace the dense region ($n(\text{H}_2) > 10^3$ cm^{-3}). The integrated ^{13}CO intensity map detects only the condensation “conds1,” which contains the *Herschel* clump1 (see Figure 8(b)). This suggests that the conds1 is the densest molecular condensation compared to the other three condensations (i.e., conds2–4). Using the integrated ^{13}CO intensity map (see Figure 11(b)), we compute the mass of the molecular condensation “conds1” to be about $242 M_{\odot}$, which is in agreement with the clump mass estimated using the *Herschel* data. In the calculation, we use an excitation temperature of 20 K, an abundance ratio ($N(\text{H}_2)/N(^{13}\text{CO})$) of 7×10^5 , and a ratio of gas to hydrogen by mass of about 1.36. One can find more details about the clump mass estimation in Yan et al. (2016) (see Equations (4) and (5) in Yan et al. 2016). The position–velocity diagrams of the ^{13}CO emission clearly indicate the presence of a velocity gradient along the condensation “conds1” (see Figures 11(d) and (f)). The

condensation “conds1” hosts a cluster of young populations (see Section 3.5.2) and filamentary features. Therefore, one can suspect the presence of molecular outflows in the condensation “conds1” (also see channel maps in Figure 10). The velocity gradient could also be explained as gas flowing through the filamentary features into their intersection. Due to the coarse beam of the FCRAO ^{12}CO and ^{13}CO data (beam size $\sim 45''$), we do not further explore this aspect in this work and are also unable to infer the gas distribution toward the filamentary features.

Recently, based on the molecular line data analysis and modeling work, Arce et al. (2011) suggested an inverted C-like or ring-like structure for an expanding shell/bubble in the position–velocity diagrams (see Figure 5 in Arce et al. 2011). In the S237 region, the presence of an inverted C-like structure in the position–velocity diagram can indicate an expanding shell. Additionally, as previously mentioned, the S237 H II region is excited by a single source of radio spectral type B0.5V. Hence, it appears that the S237 region is associated with an expanding H II region with an expansion velocity of the gas of ~ 1.65 km s^{-1} .

Altogether, the FCRAO ^{12}CO and ^{13}CO data suggest the presence of an expanding H II region.

3.5. YSOs in S237

3.5.1. Identification of YSOs

The GLIMPSE360, UKIDSS GPS, and 2MASS data allow us to investigate the infrared-excess sources present in the S237 region. In the following, we describe the YSO identification and classification schemes.

1. To identify infrared-excess sources, Gutermuth et al. (2009) described various conditions using the H , K , $3.6 \mu\text{m}$, and $4.5 \mu\text{m}$ data and utilized the dereddened color–color space ($[K-[3.6]]_0$ and $[[3.6]-[4.5]]_0$). Using the GLIMPSE360, UKIDSS GPS, and 2MASS catalogs, these dereddened colors were determined using the color-excess ratios given in Flaherty et al. (2007). This dereddened color–color space is also used to identify possible dim extragalactic contaminants from YSOs with additional conditions (i.e., $[3.6]_0 < 15$ mag for Class I and $[3.6]_0 < 14.5$ mag for Class II). The observed color and the reddening laws (from Flaherty et al. 2007) are utilized to compute the dereddened $3.6 \mu\text{m}$ magnitudes. This scheme yields 80 (7 Class I and 73 Class II) YSOs (see Figure 12(a)).

2. We find that some sources have detections only in the H and K bands. To further select infrared-excess sources from this selected population, we utilized a color–magnitude ($H-K/K$) diagram (see Figure 12(b)). The diagram depicts the red sources with $H-K > 0.65$ mag. This color criterion is selected based on the color–magnitude analysis of the nearby control field. We identify 18 additional YSO candidates using this scheme in our selected region.

Using the UKIDSS, 2MASS, and GLIMPSE360 data, a total of 98 YSOs are obtained in the selected region. The positions of all YSOs are shown in Figure 13(a).

3.5.2. Spatial Distribution of YSOs

Using the nearest-neighbor (NN) technique, the surface density analysis of YSOs is a popular method to examine their spatial distribution in a given star-forming region (e.g., Gutermuth et al. 2009; Bressert et al. 2010; Dewangan et al. 2015), which can be used to find the young stellar clusters.

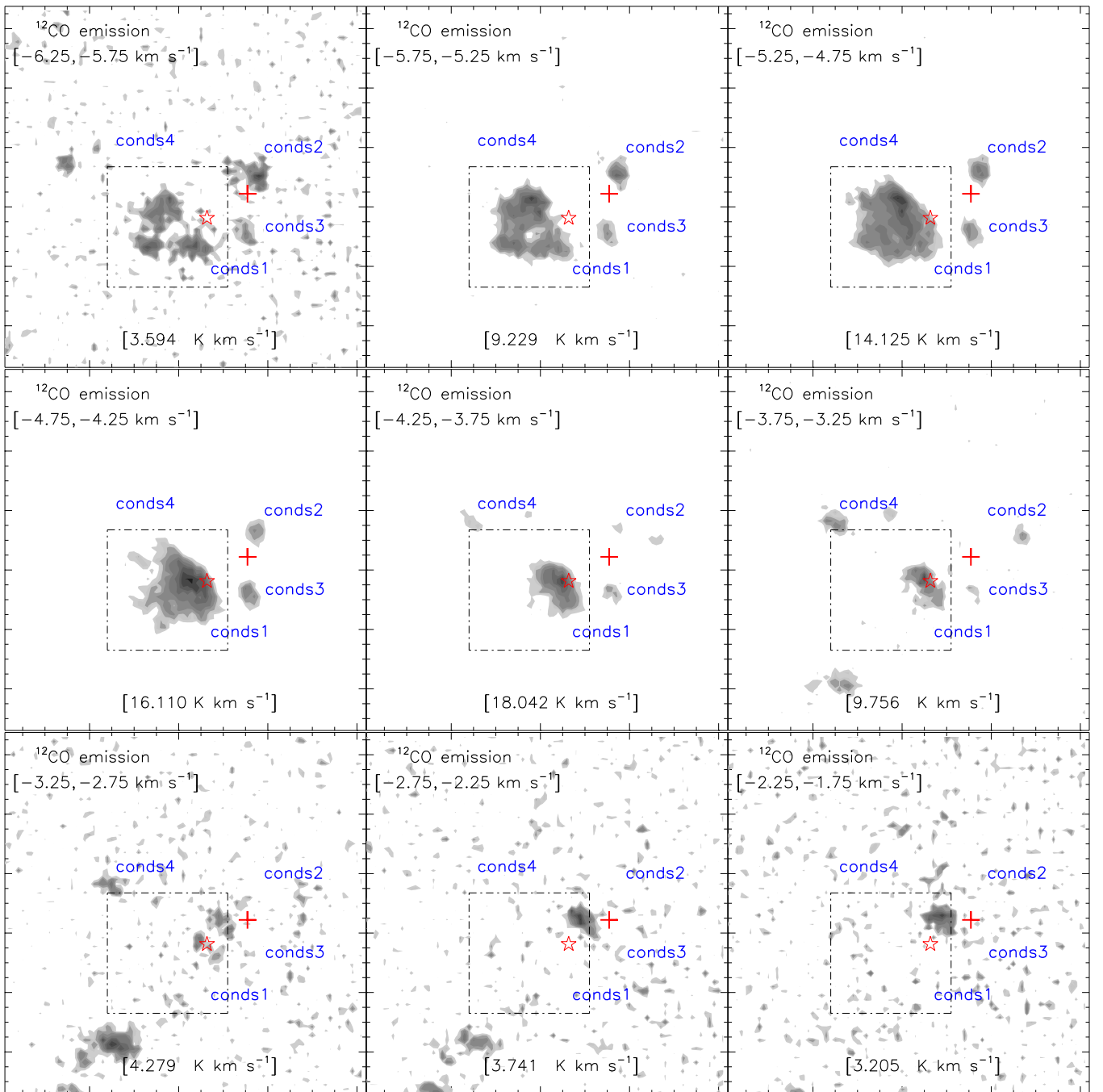


Figure 9. Velocity channel contour maps of $^{12}\text{CO}(J=1-0)$ emission. The molecular emission is integrated over a velocity interval, which is labeled in each panel (in km s^{-1}). The contour levels are 18%, 25%, 30%, 40%, 55%, 70%, 80%, 90%, and 99% of the peak value (in K km s^{-1}), which is also given in each panel. In each panel, the positions of IRAS 05281+3412 and *Herschel* column density peak are marked by a plus sign and a star, respectively. The dot-dashed black box encompasses the area shown in Figures 10 and 14. In the maps, at least four noticeable condensations (i.e., conds1–4) are observed, and the majority of molecular gas is found toward the condensation conds1.

Using the NN method, we obtain the surface density map of YSOs in a manner similar to that described in Dewangan et al. (2015) (also see equation in Dewangan et al. 2015). The surface density map of all the selected 98 YSOs was constructed, using a $5''$ grid and six NNs at a distance of 2.3 kpc. In Figure 13(b), the surface density contours of YSOs are presented and are drawn at 3, 5, 7, 10, 15, and 20 YSOs pc^{-2} , increasing from the outer to the inner regions. In Figure 13(b), two clusters of YSOs are observed in the S237

region and are mainly seen toward the *Herschel* clump1, clump2, and subreg1 (see Figure 13(b)). However, one cluster of YSOs seems to be linked with the *Herschel* clump2 and the subreg1 together. In Section 3.3, we have seen that the filamentary features and bell-shaped cavity are observed toward the *Herschel* clump1 and clump2, respectively. Hence, in the S237 region, the star formation activities are found toward the filamentary features, bell-shaped cavity, and subreg1 (see Figure 13(b)). Recently, Pandey et al. (2013) also identified

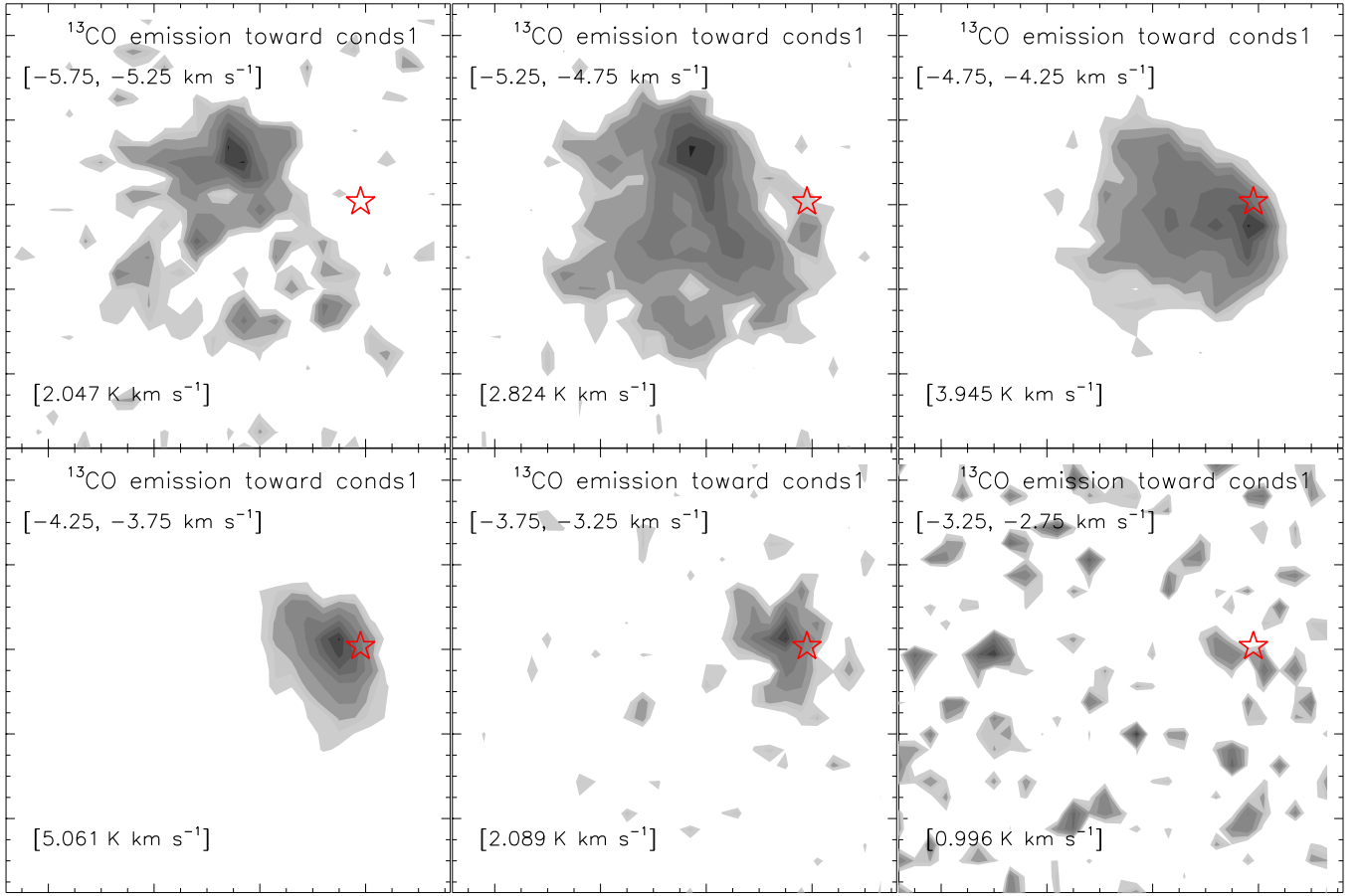


Figure 10. $^{13}\text{CO}(J = 1-0)$ velocity channel contour maps toward the molecular condensation cond1 (see dot-dashed black box in Figure 9). The molecular emission is integrated over a velocity interval, which is labeled in each panel (in km s^{-1}). The contour levels are 18%, 25%, 30%, 40%, 55%, 70%, 80%, 90%, and 99% of the peak value (in K km s^{-1}), which is also given in each panel. In each panel, the position of the *Herschel* column density peak is marked by a star.

young populations in the S237 region using the optical and NIR ($1-5 \mu\text{m}$) data. Based on the spatial distribution of young populations, they found most of the YSOs distributed mainly toward the bell-shaped cavity, subreg1, and filamentary features (see Figure 15 in Pandey et al. 2013), which was also reported by Lim et al. (2015; see their Figure 8). Furthermore, Lim et al. (2015) found an elongated shape of the surface density contours of PMS sources that is very similar in morphology to that investigated in this work. Taken together, these previous results are in a good agreement with our presented results.

In the molecular condensation cond1, the filamentary features are physically associated with a cluster of YSOs, a massive clump (having the highest column density, i.e., $3.6 \times 10^{21} \text{ cm}^{-2}$), and molecular gas (see Figure 14). Interestingly, this result suggests the role of filaments in the star formation process.

3.6. Feedback of a Massive Star

Based on the radio continuum data analysis, we find that the S237 region is powered by a radio spectral type of B0.5V star. To study the feedback of a massive star in its vicinity, we compute the three pressure components (i.e., pressure of an H II region [$P_{\text{H II}}$], radiation pressure [P_{rad}], and stellar wind ram pressure [P_{wind}]) driven by a massive star. These pressure components ($P_{\text{H II}}$, P_{rad} , and P_{wind}) are defined below (e.g.,

Bressert et al. 2012):

$$P_{\text{H II}} = \mu m_{\text{H}} c_s^2 \left(\sqrt{\frac{3N_{\text{uv}}}{4\pi \alpha_B D_s^3}} \right), \quad (4)$$

$$P_{\text{rad}} = L_{\text{bol}} / 4\pi c D_s^2, \quad (5)$$

$$P_{\text{wind}} = \dot{M}_w V_w / 4\pi D_s^2. \quad (6)$$

In the equations above, N_{uv} , c_s ($=11 \text{ km s}^{-1}$; in the ionized gas; Bisbas et al. 2009), and α_B are previously defined (see Section 3.1.2), $\mu = 0.678$ (in the ionized gas; Bisbas et al. 2009), m_{H} is the hydrogen atom mass, \dot{M}_w is the mass-loss rate, V_w is the wind velocity of the ionizing source, L_{bol} is the bolometric luminosity of the source, and D_s is the projected distance from the location of the B0.5V star where the pressure components are estimated. The pressure components driven by a massive star are evaluated at $D_s = 3.5 \text{ pc}$ (i.e., the separation between the positions of the NVSS peak and clump1).

Adopting $L_{\text{bol}} = 19952 L_{\odot}$ (for a B0.5V star; Panagia 1973), $\dot{M}_w = 2.5 \times 10^{-9} M_{\odot} \text{ yr}^{-1}$ (for a B0.5V star; Oskinova et al. 2011), and $V_w = 1000 \text{ km s}^{-1}$ (for a B0.5V star; Oskinova et al. 2011) in the above equations, we compute $P_{\text{H II}} \approx 2.0 \times 10^{-11} \text{ dynes cm}^{-2}$, $P_{\text{rad}} \approx 1.7 \times 10^{-12} \text{ dynes cm}^{-2}$, and $P_{\text{wind}} \approx 1.1 \times 10^{-14} \text{ dynes cm}^{-2}$. The comparison of these pressure components indicates that the pressure of the H II region is relatively higher than the radiation pressure and the stellar wind

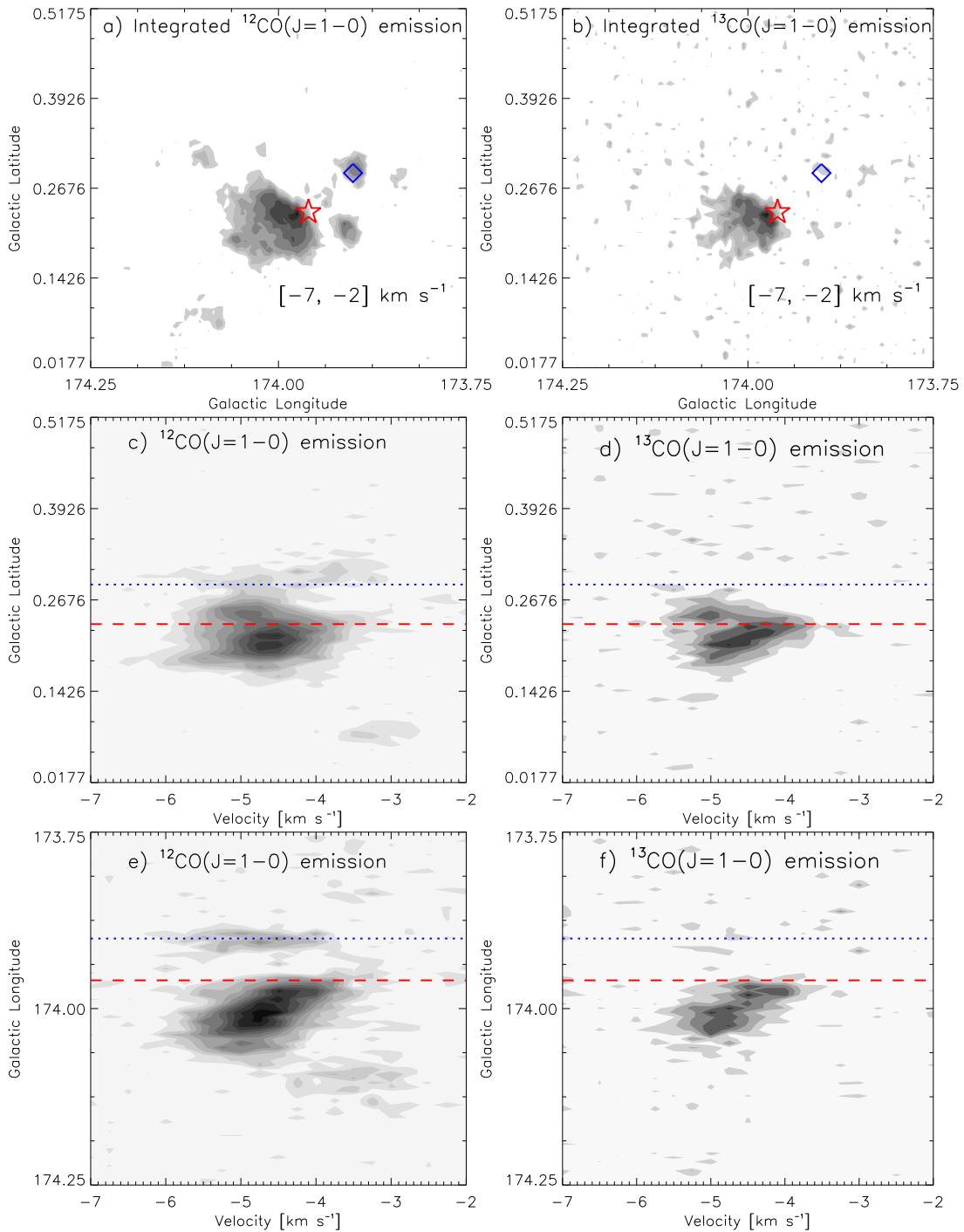


Figure 11. Distribution of ^{12}CO (left) and ^{13}CO (right) emission toward the S237 region. Top panels: contour maps of integrated (a) ^{12}CO and (b) ^{13}CO emission in the velocity range of -7 to -2 km s^{-1} . The ^{12}CO map is similar to the one shown in Figure 2(b). In the top panels, the positions of the NVSS 1.4 GHz peak emission and the *Herschel* column density peak are shown by a blue diamond and a red star, respectively. Middle panels: latitude–velocity diagrams of (c) ^{12}CO and (d) ^{13}CO . In the latitude–velocity diagrams, the molecular emission is integrated over the longitude from $173^{\circ}75$ to $174^{\circ}25$. Bottom panels: longitude–velocity diagrams of (e) ^{12}CO and (f) ^{13}CO . In the longitude–velocity diagrams, the molecular emission is integrated over the latitude from $0^{\circ}0177$ to $0^{\circ}5175$. In the position–velocity diagrams, the dotted blue and dashed red lines show the positions of the NVSS 1.4 GHz peak emission and the *Herschel* column density peak, respectively. In panel (e), the longitude–velocity diagram depicts an inverted C-like morphology, indicating the expanding shell with an expanding gas velocity of ~ 1.65 km s^{-1} . The position–velocity diagrams of ^{12}CO and ^{13}CO also trace a noticeable velocity gradient along the *Herschel* clump1, which contains the *Herschel* column density peak (also see the text).

pressure. We also obtain a total pressure ($P_{\text{total}} = P_{\text{H II}} + P_{\text{rad}} + P_{\text{wind}}$) driven by a massive star of $\sim 2.2 \times 10^{-11}$ dynes cm^{-2} . P_{total} is comparable to the pressure associated with a typical cool molecular cloud ($P_{\text{MC}} \sim 10^{-11}$ – 10^{-12} dynes cm^{-2} for a

temperature of ~ 20 K and particle density of $\sim 10^3$ – 10^4 cm^{-3} ; see Table 7.3 of Dyson & Williams 1980, p. 204), suggesting that the clump1 is not destroyed by the impact of the ionized gas.

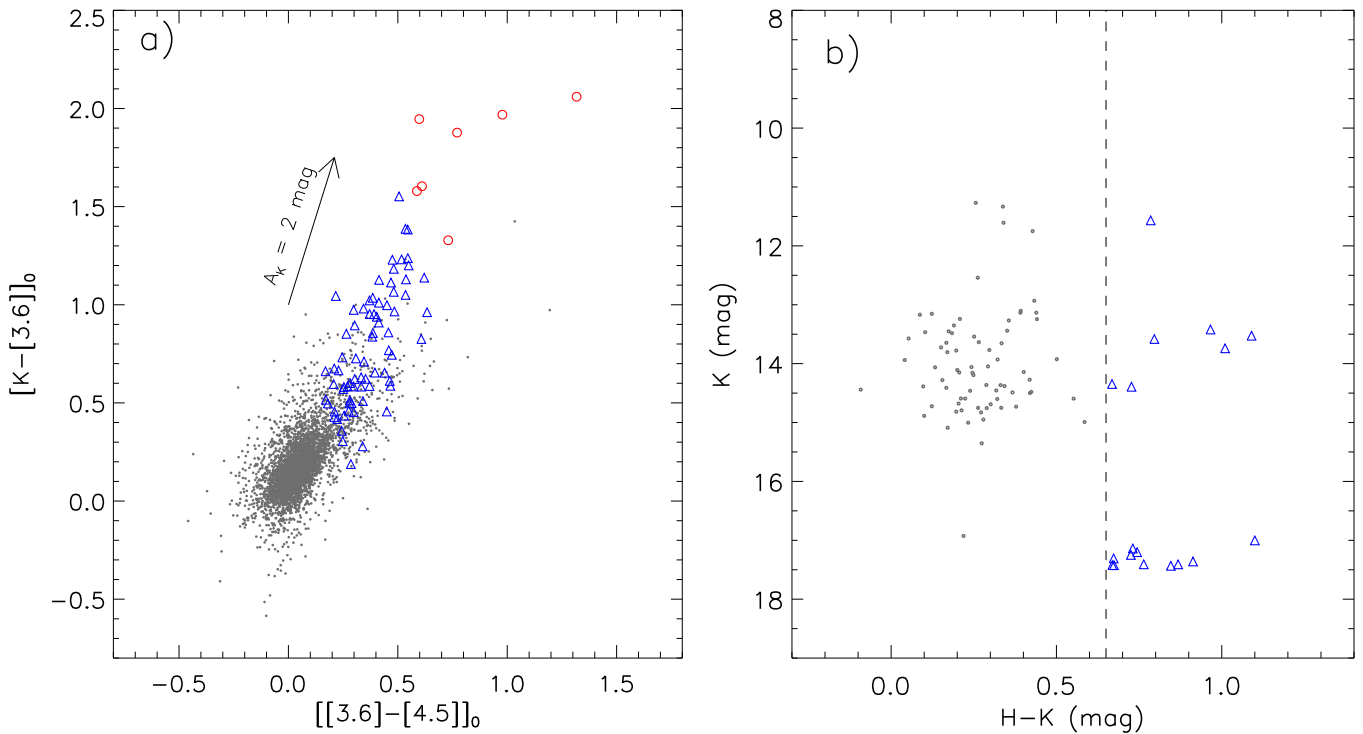


Figure 12. Selection of embedded young stellar population within the region probed in this paper (see Figure 1). (a) Dereddened $[K-[3.6]]_0$ vs. $[[3.6]-[4.5]]_0$ color-color diagram using the H , K , $3.6 \mu\text{m}$, and $4.5 \mu\text{m}$ data. The extinction vector is drawn using the average extinction laws from Flaherty et al. (2007). (b) Color-magnitude diagram ($H-K/K$) of the sources only detected in H and K bands that have no counterparts in our selected GLIMPSE360 catalog. In both panels, Class I and Class II YSOs are marked by red circles and open blue triangles, respectively. In both panels, the gray dots refer to the stars with only photospheric emissions. The positions of all the identified YSOs are shown in Figure 13(a).

4. DISCUSSION

In recent years, *Spitzer* and *Herschel* data have observed MIR shells or bubbles, infrared filaments, and young star clusters together in many massive star-forming regions, indicating the onset of numerous complex physical processes. The presence of bubbles/shells associated with H II regions is often explained by the feedback mechanisms (such as ionizing radiation, stellar winds, and radiation pressure) of massive stars (e.g., Zinnecker & Yorke 2007; Deharveng et al. 2010; Tan et al. 2014; Dewangan et al. 2015). The multiband images have revealed an almost sphere-like shell morphology as the most prominent structure in the S237 region. The shell-like HISA feature surrounding the ionized emission is also seen in the 21 cm H I line data. The velocity structure of molecular gas has indicated the presence of an expanding H II region associated with the S237 region (see Section 3.4). Additionally, in Section 3.6, based on the pressure calculations ($P_{\text{H II}}$, P_{rad} , and P_{wind}), we find that the photoionized gas linked with the S237 H II region can be considered as the major contributor (against stellar winds and radiation pressure) for the feedback process in the S237 region. Hence, the presence of a bell-shaped cavity-like morphology could be explained by the impact of ionizing photons (see Section 3.2).

In Section 3.5.2, we detect only two clusters of YSOs in the S237 region. Thirteen *Herschel* clumps are identified in the S237 region, and star formation activities are exclusively found toward the *Herschel* clump1 and clump2 (see Section 3.5.2). Interestingly, clump1 and clump2 contain the bell-shaped cavity-like structure hosting the peaks of 1.4 GHz emission and diffuse $H\alpha$ emission and filamentary features without any radio continuum detection, respectively. Lim et al. (2015) also found

two groups of PMS stars inferred using their surface density analysis and estimated a median age of PMS members of 2.0 Myr. They also reported the maximum age difference between the stars in these two groups to be about 0.7 Myr, on average. Considering the presence of the expanding H II region, the spatial locations of the YSO clusters may indicate the triggered star formation scenario in the S237 region. One can obtain more details about different processes of triggered star formation in the review article by Elmegreen (1998). Evans et al. (2009) reported an average age of the Class I and Class II YSOs of ~ 0.44 Myr and $\sim 1-3$ Myr, respectively. Comparing these typical ages of YSOs with the dynamical age of the S237 H II region (i.e., $\sim 0.2-0.8$ Myr; see Section 3.1.2), it seems that the S237 H II region is too young for initiating the formation of a new generation of stars. This is also supported by the results obtained by Lim et al. (2015) (see above). Hence, the young clusters are unlikely to have been the product of triggered formation. The ^{13}CO emission is not detected toward clump2 and subreg1, indicating the absence of dense gas toward these subregions (see Figure 11(b)). Note that the hot gas emission is traced toward subreg1 using the *ROSAT* X-ray image and is found away (about $2'$) from the 1.4 GHz peak emission. The surface density contours are also seen toward subreg1. We suspect that the diffuse X-ray emission could originate from young stars present in the cluster (see subreg1 in Figure 5(a)). Due to coarse resolution of the *ROSAT* X-ray image, we cannot identify the X-ray-emitting young stars. In general, Elmegreen (2011) mentioned that open cluster complexes could be the remnants of star formation in giant clouds formed by gravitational instabilities in the Milky Way gas layer.

It is also worth mentioning that the *Herschel* clump1 is the most massive, with about $260 M_{\odot}$, contains the filamentary

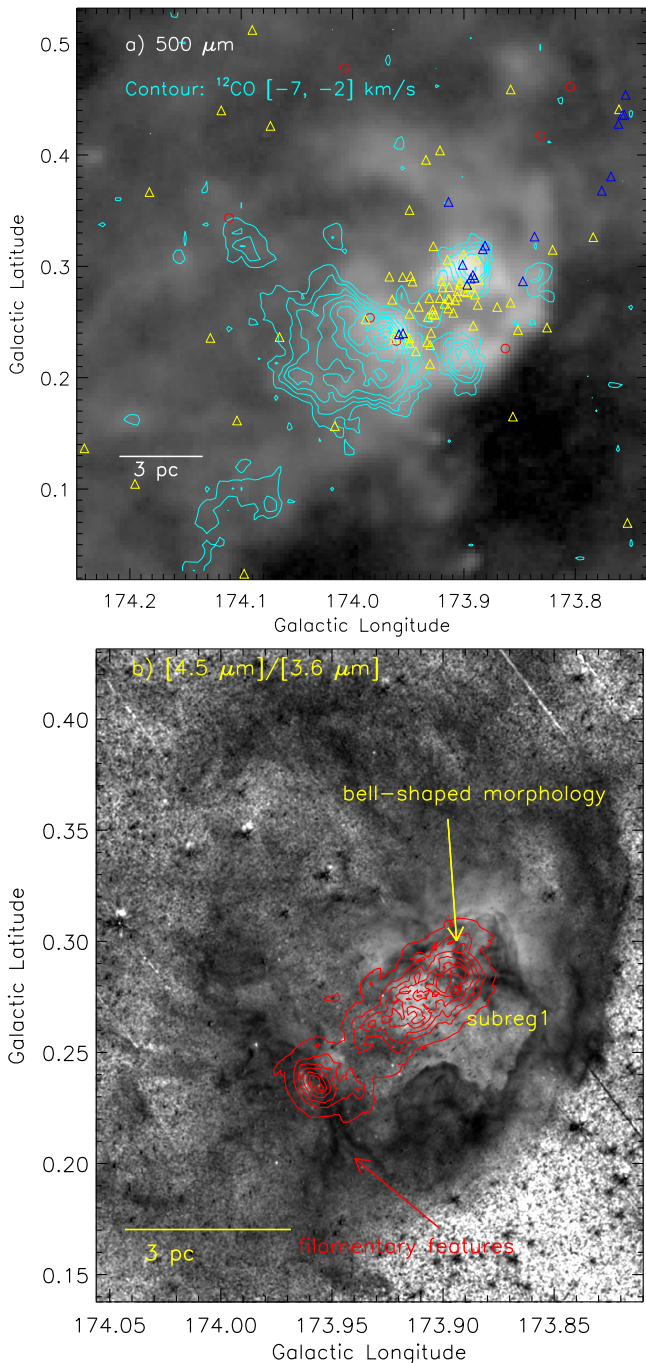


Figure 13. Spatial distribution of YSOs identified within the region probed in this paper using the NIR ($1\text{--}5\ \mu\text{m}$) data. (a) The ^{12}CO emission and the positions of YSOs are overlaid on the *Herschel* $500\ \mu\text{m}$ map. The background map is similar to the one shown in Figure 2. The positions of Class I and Class II YSOs identified within our selected region are shown by circles (in red) and triangles (in blue and yellow), respectively. The YSOs selected using the H , K , $3.6\ \mu\text{m}$, and $4.6\ \mu\text{m}$ data (see Figure 12(a)) are shown by red circles and yellow triangles, whereas the blue triangles represent the YSOs identified using the H and K bands (see Figure 12(b)). (b) The surface density contours (in red) of all the identified YSOs are overlaid on the *Spitzer* IRAC ratio map of $4.5\ \mu\text{m}/3.6\ \mu\text{m}$ emission (similar area to that shown in Figure 3(a)), indicating the star formation activities mainly toward the filamentary features/clump1 and the bell-shaped morphology/clump2 (see text for details). The contours are shown at 3, 5, 7, 10, 15, and 20 YSOs pc^{-2} , from the outer to the inner side. In both panels, the scale bar at the bottom left corner corresponds to 3 pc (at a distance of 2.3 kpc).

features, and has a noticeable velocity gradient in both the ^{12}CO and ^{13}CO emissions. In Figure 14, there is convincing evidence for a physical association of a cluster of YSOs and a massive clump with the filamentary features, indicating the role of filaments in the star formation process. Recently, Nakamura et al. (2014) studied the filamentary ridges in the Serpens South infrared dark cloud using the molecular line observations and argued that the filamentary ridges appeared to converge toward the protocluster clump. Furthermore, they suggested that the collisions of the filamentary ridges may have triggered cluster formation. Schneider et al. (2012) also carried out *Herschel* data analysis toward the Rosette Molecular Cloud and suggested that the infrared clusters were preferentially seen at the junction of filaments or filament mergers. They also reported that their outcomes are in agreement with the results obtained in the simulations of Dale & Bonnell (2011). In the present work, due to coarse beam sizes of the molecular line data, we cannot directly probe the converging of filaments toward the protocluster clump. Here, a protocluster clump refers to a massive clump associated with a cluster of YSOs without any radio continuum emission. However, our results indicate the presence of a cluster of YSOs and a massive clump at the intersection of filamentary features, similar to those found in the Serpens South region. Therefore, it seems that the collisions of these features may have influenced the cluster formation. Based on these indicative outcomes, further detailed investigation of this region is encouraged using high-resolution molecular line observations.

In general, the information of the relative orientation of the mean field direction and the filamentary features allows us to infer the role of magnetic fields in the formation and evolution of the filamentary features. Using previous optical polarimetric observations (from Pandey et al. 2013), we find an average value of the equatorial position angle of three stars of $161^\circ.5$, which are located near the filamentary features (see the positions of these stars in Figure 14(b)), while the equatorial position angle of the filamentary features at their intersection zone is computed to be about 95° . The polarization vectors of background stars indicate the magnetic field direction in the plane of the sky parallel to the direction of polarization (Davis & Greenstein 1951). Hence, these filamentary features seem to be nearly perpendicular to the plane-of-the-sky projection of the magnetic field linked to the molecular condensation cond1 in the S237 region, indicating that the magnetic field is likely to have influenced the formation of the filamentary features. Sugitani et al. (2011) studied NIR imaging polarimetry toward the Serpens South cloud and found that the magnetic field is nearly perpendicular to the main filament. In particular, the filamentary features in the S237 region appear to originate from a similar process to that observed in the Serpens South cloud. However, high-resolution polarimetric observations at longer wavelengths will be helpful to further explore the role of magnetic field in the formation of the filamentary features in the S237 region.

5. SUMMARY AND CONCLUSIONS

In order to investigate star formation processes in the S237 region, we have utilized multiwavelength data covering radio, NIR, optical $H\alpha$, and X-ray wavelengths. Our analysis has been focused on the molecular gas kinematics, ionized

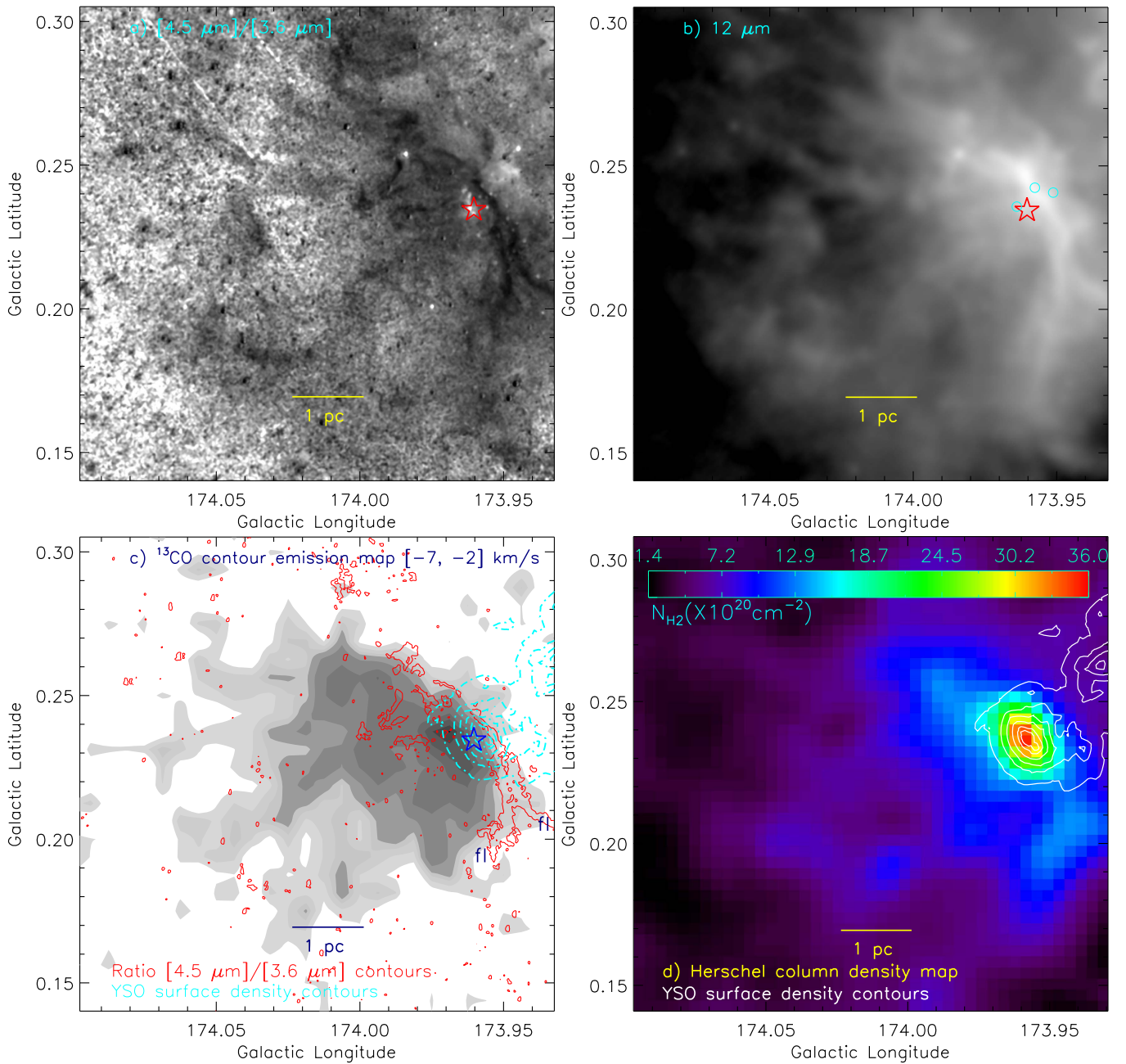


Figure 14. Zoomed-in view toward the molecular condensation cond1, as traced in the integrated ^{12}CO and ^{13}CO maps (see dot-dashed box in Figure 9). (a) *Spitzer* IRAC ratio map of $4.5 \mu\text{m}/3.6 \mu\text{m}$ emission traces the filamentary features. (b) *WISE* image at $12 \mu\text{m}$ also depicts the filamentary features. The positions of three stars having optical polarimetric observations (from Pandey et al. 2013) are marked by cyan circles. (c) Integrated ^{13}CO ($J=1-0$) emission map of the molecular condensation cond1. The ^{13}CO contours are shown with levels of 10%, 18%, 25%, 30%, 40%, 55%, 70%, 80%, 90%, and 99% of the peak value (i.e., $8.251 \text{ K km s}^{-1}$). The YSO surface density contours (dot-dashed; in cyan color) and filamentary features (in red) are also shown in the map. Two filamentary features are highlighted by labels “fl.” (d) *Herschel* column density map overlaid with the YSO surface density contours, revealing a physical connection between a cluster of YSOs and a massive clump. In the last two panels, the contours are shown at 3, 5, 7, 10, 15, and 20 YSOs pc^{-2} , from the outer to the inner side. In the first three panels, the position of the *Herschel* column density peak is marked by a star. The panels exhibit the presence of a cluster of YSOs and a massive clump at the intersection of filamentary features.

emission, hot gas, cold dust emission, and embedded young populations. Our main findings are as follows:

(1) The S237 region has a broken or incomplete ring- or shell-like appearance at wavelengths longer than $2 \mu\text{m}$ and contains a prominent bell-shaped cavity-like morphology at the center, where the peak of the radio continuum emission is observed. The elongated filamentary features are also seen at the edge of the shell-like structure, where the radio continuum emission is absent.

(2) The distribution of ionized emission traced in the NVSS 1.4 GHz continuum map is almost spherical, and the S237 H II region is powered by a radio spectral type of B0.5V star. The dynamical age of the S237 H II region is estimated to be ~ 0.2 (0.8) Myr for 10^3 (10^4) cm^{-3} ambient density.

(3) The molecular cloud associated with the S237 region (i.e., S237 molecular cloud) is well traced in a velocity range of -7 to -2 km s^{-1} . In the integrated ^{12}CO map, at least four molecular condensations (conds1–4) are identified.

(4) In the integrated ^{13}CO map, the molecular gas is seen only toward the condensation cond1.

(5) Using the 0.5–2 keV X-ray image, the hot gas emission is traced at the center of the shell-like morphology and could be due to young stars present in the cluster.

(6) The position–velocity analysis of ^{12}CO emission depicts an inverted C-like structure, revealing the signature of an expanding H II region with a velocity of $\sim 1.65 \text{ km s}^{-1}$.

(7) The pressure calculations ($P_{\text{H II}}$, P_{rad} , and P_{wind}) indicate that the photoionized gas associated with the S237 H II region could be responsible for the origin of the bell-shaped structure seen in the S237 region.

(8) Thirteen *Herschel* clumps have been traced in the *Herschel* column density map. The majority of molecular gas is distributed toward the massive *Herschel* clump1 ($M_{\text{clump}} \sim 260 M_{\odot}$), which contains the filamentary features. The position–velocity analysis of ^{12}CO and ^{13}CO emission traces a noticeable velocity gradient along this *Herschel* clump1.

(9) The analysis of NIR (1–5 μm) photometry provides a total of 98 YSOs and also traces the clusters of YSOs mainly toward the bell-shaped structure and the filamentary features.

(10) Toward the elongated filamentary features, a cluster of YSOs is spatially coincident with the massive *Herschel* clump1 embedded within the molecular condensation cond1.

Taking into account the lower dynamical age of the H II region (i.e., 0.2–0.8 Myr), the clusters of YSOs are unlikely to originate from the expansion of the H II region. An interesting outcome of this work is the existence of a cluster of YSOs and a massive clump at the intersection of filamentary features, indirectly illustrating that the collisions of these features may have triggered cluster formation, similar to those seen in the Serpens South star-forming region.

We thank the anonymous reviewer for a critical reading of the manuscript and several useful comments and suggestions, which greatly improved the scientific contents of the paper. The research work at the Physical Research Laboratory is funded by the Department of Space, Government of India. This work is based on data obtained as part of the UKIRT Infrared Deep Sky Survey. This publication made use of data products from the Two Micron All Sky Survey (a joint project of the University of Massachusetts and the Infrared Processing and Analysis Center/California Institute of Technology, funded by NASA and NSF) and archival data obtained with the *Spitzer Space Telescope* (operated by the Jet Propulsion Laboratory, California Institute of Technology, under a contract with NASA). The Canadian Galactic Plane Survey (CGPS) is a Canadian project with international partners. The Dominion Radio Astrophysical Observatory is operated as a national facility by the National Research Council of Canada. The Five College Radio Astronomy Observatory CO Survey of the Outer Galaxy was supported by NSF grant AST 94-20159. The CGPS is supported by a grant from the Natural Sciences and Engineering Research Council of Canada. This paper makes use of data obtained as part of the INT Photometric $\text{H}\alpha$ Survey of the Northern Galactic Plane (IPHAS, www.iphas.org) carried out at the Isaac Newton Telescope (INT). The INT is operated on the island of La Palma by the Isaac Newton Group in the Spanish Observatorio del Roque de los Muchachos of the Instituto de Astrofísica de Canarias. All IPHAS data are processed by the Cambridge Astronomical Survey Unit, at the

Institute of Astronomy in Cambridge. I.Z. is supported by the Russian Foundation for Basic Research (RFBR). A.L. acknowledges the CONACYT(México) grant CB-2012-01-1828-41. We have made use of the *ROSAT* Data Archive of the Max-Planck-Institut für extraterrestrische Physik (MPE) at Garching, Germany.

REFERENCES

- André, P., Men'shchikov, A., Bontemps, S., et al. 2010, *A&A*, **518**, L102
- Arce, H. G., Borkin, M. A., Goodman, A. A., Pineda, J. E., & Beaumont, C. N. 2011, *ApJ*, **742**, 105
- Baker, P. L., & Burton, W. B. 1979, *A&AS*, **35**, 129
- Balsler, D. S., Rood, R. T., Bania, T. M., & Anderson, L. D. 2011, *ApJ*, **738**, 27
- Bisbas, T. G., Wunsch, R., Whitworth, A. P., & Hubber, D. A. 2009, *A&A*, **497**, 649
- Bohlin, R. C., Savage, B. D., & Drake, J. F. 1978, *ApJ*, **224**, 13233
- Bressert, E., Bastian, N., Gutermuth, R., et al. 2010, *MNRAS*, **409**, 54
- Bressert, E., Ginsburg, A., Bally, J., et al. 2012, *ApJ*, **758**, 28
- Brunt, C. 2004, in Proc. ASP Conf. 317, Milky Way Surveys: The Structure and Evolution of Our Galaxy, ed. D. Clemens, R. Shah, & T. Brainerd (San Francisco, CA: ASP), 79
- Burton, W. B., & Liszt, H. S. 1981, in IAU Symp. 94, Origin of Cosmic Rays, ed. G. Setti, G. Spada, & A. W. Wolfendale (Dordrecht: Reidel), 227
- Burton, W. B., Liszt, H. S., & Baker, P. L. 1978, *ApJ*, **219**, 67
- Casali, M., Adamson, A., Alves de Oliveira, C., et al. 2007, *A&A*, **467**, 777
- Condon, J. J., Cotton, W. D., Greisen, E. W., et al. 1998, *AJ*, **115**, 1693
- Dale, J. E., & Bonnell, I. A. 2011, *MNRAS*, **414**, 321
- Davis, L., Jr., & Greenstein, J. L. 1951, *ApJ*, **114**, 206
- Deharveng, L., Schuller, F., Anderson, L. D., et al. 2010, *A&A*, **523**, 6
- Dewangan, L. K., & Anandarao, B. G. 2011, *MNRAS*, **414**, 1526
- Dewangan, L. K., Luna, A., Ojha, D. K., et al. 2015, *ApJ*, **811**, 79
- Dewangan, L. K., Ojha, D. K., Anandarao, B. G., Ghosh, S. K., & Chakraborti, S. 2012, *ApJ*, **756**, 151
- Dewangan, L. K., Ojha, D. K., Luna, A., et al. 2016, *ApJ*, **819**, 66
- Drew, J. E., Greimel, R., Irwin, M. J., et al. 2005, *MNRAS*, **362**, 753
- Dyson, J. E., & Williams, D. A. 1980, *Physics of the Interstellar Medium* (New York: Halsted Press)
- Elmegreen, B. G. 1998, in ASP Conf. Ser. 148, Origins, ed. C. E. Woodward, J. M. Shull, & H. A. Thronson, Jr. (San Francisco, CA: ASP), 150
- Elmegreen, B. G. 2011, in EAS Publications Ser. 51, Star Formation in the Local Universe, ed. C. Charbonnel & T. Montmerle (Les Ulis: EDP), 31
- Evans, N. J., II, Dunham, M. M., Jørgensen, J. K., et al. 2009, *ApJS*, **181**, 321
- Flaherty, K. M., Pipher, J. L., Megeath, S. T., et al. 2007, *ApJ*, **663**, 1069
- Glushkov, Y. I., Denisyuk, E. K., & Karyagina, Z. V. 1975, *A&A*, **39**, 481
- Griffin, M. J., Abergel, A., Abreu, A., et al. 2010, *A&A*, **518**, L3
- Gutermuth, R. A., Megeath, S. T., Myers, P. C., et al. 2009, *ApJS*, **184**, 18
- Heyer, M., Brunt, C., Snell, R., et al. 1998, *ApJS*, **115**, 241
- Heyer, M. H., Carpenter, J. M., & Ladd, E. F. 1996, *ApJ*, **463**, 630
- Hildebrand, R. H. 1983, *QJRAS*, **24**, 267
- Kauffmann, J., Bertoldi, F., Bourke, T. L., Evans, N. J., II, & Lee, C. W. 2008, *ApJ*, **487**, 993
- Kerton, C. R. 2005, *ApJ*, **623**, 235
- Krumholz, M. R., & McKee, C. F. 2008, *Natur*, **451**, 1082
- Kwan, J. 1997, *ApJ*, **489**, 284
- Lawrence, A., Warren, S. J., Almaini, O., et al. 2007, *MNRAS*, **379**, 1599
- Leisawitz, D., Bash, F. N., & Thaddeus, P. 1989, *ApJS*, **70**, 731
- Lim, B., Sung, H., Bessell, M. S., et al. 2015, *AJ*, **149**, 127
- Liszt, H. S., Burton, W. B., & Bania, T. M. 1981, *ApJ*, **246**, 74
- Lucas, P. W., Hoare, M. G., Longmore, A., et al. 2008, *MNRAS*, **391**, 1281
- Mallick, K. K., Ojha, D. K., Tamura, M., et al. 2015, *MNRAS*, **447**, 2307
- Matsakis, D. N., Evans, N. J., II, Sato, T., & Zuckerman, B. 1976, *AJ*, **81**, 172
- Molinari, S., Swinyard, B., Bally, J., et al. 2010, *A&A*, **518**, L100
- Myers, P. C. 2009, *ApJ*, **700**, 1609
- Nakamura, F., Sugitani, K., Tanaka, T., et al. 2014, *ApJL*, **791**, L23
- Oskinova, L. M., Todt, H., Ignace, R., et al. 2011, *MNRAS*, **416**, 1456
- Ott, S. 2010, in ASP Conf. Ser. 434, Astronomical Data Analysis Software and Systems XIX, ed. Y. Mizumoto, K.-I. Morita, & M. Ohishi (San Francisco, CA: ASP), 139
- Panagia, N. 1973, *AJ*, **78**, 929
- Pandey, A. K., Eswaraiah, C., Sharma, S., et al. 2013, *ApJ*, **764**, 172
- Poglitsch, A., Waelkens, C., Geis, N., et al. 2010, *A&A*, **518**, L2
- Povich, M. S., Stone, J. M., Churchwell, E., et al. 2007, *ApJ*, **660**, 346
- Reipurth, B. (ed.) 2008, *Handbook of Star Forming Regions*, Vol. I (San Francisco, CA: ASP)

- Schneider, N., Csengeri, T., Hennemann, M., et al. 2012, [A&A](#), **540**, L11
- Skrutskie, M. F., Cutri, R. M., Stiening, R., et al. 2006, [AJ](#), **131**, 1163
- Sugitani, K., Nakamura, F., Watanabe, M., et al. 2011, [ApJ](#), **734**, 63
- Tan, J. C., Beltrán, M. T., Caselli, P., et al. 2014, in *Protostars and Planets VI*, ed. H. Beuther et al. (Tucson, AZ: Univ. Arizona Press), 149
- Taylor, A. R., Gibson, S. J., Peracaula, M., et al. 2003, [AJ](#), **125**, 3145
- Voges, W., Aschenbach, B., Boller, Th., et al. 1999, [A&A](#), **349**, 389
- Voges, W., Aschenbach, B., Boller, Th., et al. 2000, [IAUC](#), **7432**, 3
- Watson, C., Hanspal, U., & Mensistu, A. 2010, [ApJ](#), **716**, 1478
- Watson, C., Povich, M. S., Churchwell, E. B., et al. 2008, [ApJ](#), **681**, 1341
- Whitney, B., Benjamin, R., Meade, M., et al. 2011, [BAAS](#), **43**, 241.16
- Williams, J. P., de Geus, E. J., & Blitz, L. 1994, [ApJ](#), **428**, 693
- Wright, E. L., Eisenhardt, P. R. M., Mainzer, A. K., et al. 2010, [AJ](#), **140**, 1868
- Yan, Q. Z., Xu, Y., Zhang, B., et al. 2016, [arXiv:1609.03051](#)
- Yang, J., Jiang, Z., Wang, M., Ju, B., & Wang, H. 2002, [ApJS](#), **141**, 157
- Zinnecker, H., & Yorke, H. W. 2007, [ARA&A](#), **45**, 481